BL2A

The Measurement of Soft X-Ray Excited Optical Luminescence of a Ge^+ Implanted Silica Glass Sample

T. Yoshida[1], S. Muto[2] and H.Yoshida[3]

[1]*EcoTopia Science Institute, Nagoya University, Nagoya 464-8603, Japan*

[2]*Department of Materials, Physics and Energy Engineering, Nagoya University, Nagoya 464-8603, Japan*

[3]*Department of Applied Chemistry, Graduate School of Engineering, Nagoya University, Nagoya 464-8603, Japan*

The discovery of room temperature photoluminescence (PL) from indirect band gap materials has generated important interest in this field. In particular, Ge doped silica glass is expected to apply to a light emission source for communication in a LSI chip as well as to single electron devices, since it shows blue and violet electroluminescence around 3.1 eV [1, 2]. Although the Ge doped silica glass has been studied extensively, the origin of the 3.1 eV PL and the emission mechanism still remain controversial. The purpose of this paper is to discuss the relation between the optical properties and the chemical state of Ge atoms in a silica glass, applying X-ray absorption fine structures (XAFS).

The sample used in this study was a synthesized silica glass (T-4040, OH content: 800ppm) produced by Toshiba Ceramics, Japan, 13 mm in diameter and 2 mm in thickness. Mass analyzed Ge^+ ions of 30 keV were injected into the samples at room temperature normal to the sample surface. The Ge^+ fluence ranged from 2 x 10^{14} to 2 x 10^{16} cm^{-2}. The measurement of luminescence of the samples induced by soft X-ray irradiation was carried out on the beamline BL1A and BL2A at UVSOR, Institute for Molecular Science. The luminescence was focused by a lens in the UHV chamber to the monochromator (CP-200, JOBIN YVON) and detected by a multi-channel analyser (OMA III, EG&G PRINCETON APPLIED RESEARCH).

PL spectra before and after the Ge^+ implantation were measured at room temperature using a Hitachi F-4500 spectrometer.

Fig. 1 shows PL spectra excited by 5 eV light before and after Ge^+ implantation. A weak and broad band is observed before implantation, while a new emission band around 2.7 eV appears after the implantation of 2 x 10^{15} cm^{-2}. This PL band was ascribed to the $B_{2\alpha}$ oxygen deficient centers [3] associated with the displacement damages. When the fluence is more than 2 x 10^{16} cm^{-2}, a sharp and intense 3.1 eV PL band replaces the 2.7 eV band.

We tried to measure Ge $L_{2,3}$-edge XANES spectra of the 2 x 10^{16} cm^{-2} implanted sample in the total electron yield mode (TEY), but the concentration of Ge atom were too low to measure. On the other hand, we found that an intense soft X-ray induced luminescence of this sample is observed at 3.1 eV. Therefore, we measured the excitation spectra of the 3.1eV band by changing the incident energy of the soft X-ray, and show the spectra in Fig. 2 together with Ge $L_{2,3}$-edge XANES of a Ge (0) powder sample recorded in the TEY mode. It is interesting to see good correspondence among them, and this result may indicate that the Ge (0) species relate to the generation of 3.1 eV PL.

[1] L. Rebohle, J. von Borany, R. A. Yankov, W. Skorypa, I. E. Tyschenko, H. Froeb and K. Leo, Appl. Phys. Lett. **71** (19) (1997) 2809.

[2] M. L. Brongersma, A. Polman, K. S. Min, E. Boer, T. Tambo, H. A. Atwater, Appl. Phys. Lett. **72** (1998) 2577.

[3] Skuja L. N. and Etzian W., Phys. Status Solidi A **96** (1986) 191.

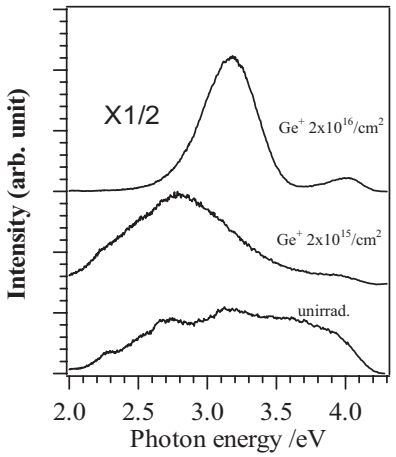

Fig. 1. PL spectra excited by 5 eV light for silica glass before and after Ge^+ implantation.

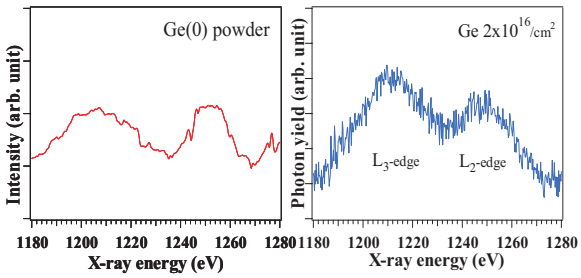

Fig. 2. Comparison between the luminescence yield spectrum of the 3.1 eV band for a silica glass irradiated by Ge^+ and Ge $L_{2,3}$-edge XANES spectrum of a Ge powder.

BL2A

Local-Structures of P of $LiMnFePO_4$ Doped with Mn

A. Nakahira[1, 2], S. Hayashi[1], M. Sato[2], Y. Takamatsu[1], Y. Nishio[1], Y. Kawabe[1], S. Misu[1], K. Kumadani[1], T. Shirai[1] and H. Aritani[3]

[1]*Faculty of Engineering, Materials Science and Engineering Dept, Osaka Prefecture University, 1-1 Gakuen-cho, Naka-ku, Sakai 599-8531, Japan*

[2]*Kansai Center, Institute of Materials Research (IMR), Tohoku University, 1-1 Gakuencho, Naka-ku, Sakai 599-8531, Japan*

[3]*Faculty of Engineering, Saitama Institute of Technology, 1690 Fusai-ji, Fukaya 369-0293, Japan*

$LiFePO_4$ (lithium iron phosphate) is an interesting alternative positive electrode material for lithium and lithium-ion rechargeable batteries application because of due to its low cost and good specific capacity. Although these $LiFePO_4$ (lithium iron phosphate) materials have some advantages in terms of environmental benignity, potential low-cost synthesis, cycling stability, and high temperature capability, the major drawback point for $LiFePO_4$ is the poor lithium ion conductivity, which have limited its power-demanding applications such as hybrid electric vehicles and other power generating equipments.

A number of various efforts has been made in the past decade to solve the conductivity problem for $LiFePO_4$. Nowadays, the main problems for $LiFePO_4$ is still the poor lithium ions conductivity caused by the low intrinsic electronic conductivity. Therefore, the modification of $LiFePO_4$ added with Mn have been attempted. In this study, $LiFePO_4$ added with Mn ($LiMnFePO_4$) was synthesized through the chemical synthesis of $LiFePO_4$ materials by the solution processing process and the heat-treatments in order to improve the specific capacity and cycling stability etc. The purpose of this study is to investigate the P-*K* edge local structures for $LiFePO_4$ added with Mn ($LiMnFePO_4$).

The synthesis of $LiFePO_4$ and $LiFePO_4$ added with Mn ($LiMnFePO_4$) was carried out using LiOH, $(NH_4)_2HPO_4$, $MnSO_4$ and $FeSO_4$, and the ascorbic acid was used as a carbon source. These stock solutions were prepared for 1 mol/L LiOH, 0.5 mol/L $(NH_4)_2HPO_4$, 0.5 mol/L $FeSO_4$ and 0.5 mol/L $MnSO_4$. The synthetic reaction was carried out through the hydrothermal treatments in autoclave bomb at various temperatures. The products were aged for various times and filtered with Buchner funnel. The products were dried at 323K for 24 hours and ground with alumina mortar. The products were characterized by XRD and FT-IR and their microstructures by SEM and TEM. The local structures around P-*K* edge for the powders of $LiFePO_4$ added with Mn ($LiMnFePO_4$) were evaluated and characterized by measuring X-ray adsorption near edge structure (XANES) at BL2A at UVSOR in Okazaki.

The components of products of $LiFePO_4$ added with Mn ($LiMnFePO_4$) were evaluated by XRD and the products were identified to be olivine type $LiFePO_4$. Figure 1 shows the results of P-*K* edge for the powders of $LiFePO_4$ added with Mn ($LiMnFePO_4$). The P-*K* edge of $(NH_4)_2HPO_4$ was measured as a reference material. The peaks of $LiFePO_4$ and $LiFePO_4$ added with Mn ($LiMnFePO_4$) were higher than $(NH_4)_2HPO_4$ as a reference material. Furthermore, $LiFePO_4$ added with Mn ($LiMnFePO_4$) had the higher energy of P-*K* edge peak, compared to monolithic$LiFePO_4$. It is obvious that the peak shift of P-*K* edge for $LiFePO_4$ added with Mn ($LiMnFePO_4$) was attributed to the addition of Mn into $LiFePO_4$.

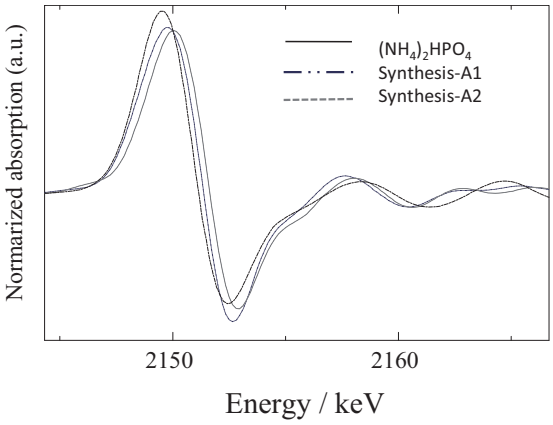

Fig. 1. XANES results of P-*K* edge for $LiFePO_4$ added with Mn ($LiMnFePO_4$).

BL2A

Evaluation of Al Local Structure of Cu-Al based Talcite Clay

A. Nakahira[1, 2], S. Hayashi[1], M. Sato[2], Y. Takamatsu[1], S. Misu[1], K. Kumadani[1] and H. Aritani[3]

[1]*Faculty of Engineering, Materials Science and Engineering Dept, Osaka Prefecture University, 1-1 Gakuen-cho, Naka-ku, Sakai 599-8531, Japan*

[2]*Kansai Center, Institute of Materials Research (IMR), Tohoku University, 1-1 Gakuencho, Naka-ku, Sakai 599-8531, Japan*

[3]*Faculty of Engineering, Saitama Institute of Technology, 1690 Fusai-ji, Fukaya 369-0293, Japan*

Hydrotalcite is one of unique clay minerals among the layered double hydroxide (LDH) materials, which are composed of double layered structures, its composition formula of $[M^{2+}_{1-X}\ M^{3+}_{X}\ (OH)_2 \cdot A^{n-}_{X/n} \cdot nH_2O]$. These materials are expected to be useful due to wide potentials as filers, catalysis, drug delivery system (DDS) and adsorption materials. "MgAl-talcie basically composed of Mg^{2+} and Al^{3+}, which is called hydrotalcite, is most popular among LDH materials .

In order to improve various properties of LDH, especially Mg-Al LDH (hydrotalcite), recently, the developments of novel LDH materials modified with the substitution of Mg^{2+} and Al^{3+} sites with another M^{2+} and M^{3+}, are attempted for expanding the new application fields. We also have developed the new types of LDH materials modified with the addition of Zn^{2+}, Ni^{2+}, Fe^{3+} and other cations of M^{2+} and M^{3+}. In this study, we successfully synthesized the novel LDH materials composed of Cu^{2+}-Al^{3+} based hydrotalcite by the soft solution process (co-precipitation processing). Therefore, we, here, attempted to investigate the Al local structure of Cu^{2+}-Al^{3+} based hydrotalcite with the X-ray adsorption near edge structure (XANES) measurements to clarify of the fine structure.

The stock solutions of 0.2 mol/dm^3 $CuCl_2$ aqueous solution. 0.1 mol/dm^3 $AlCl_3$ aqueous solution, and 0.05 mol/dm^3 $NaHCO_3$ were prepared. The pH of mixing solution was controlled with the NaHCO3 solution and aqueous NaOH solution. The products were synthesized by the co-precipitation method as a soft chemical process. CuAl-talcite with M^{2+}/M^{3+} =2~4 were synthesized by adding mixing solution into 0.05 mol/dm^3 $NaHCO_3$ at RT. 1 mol/dm^3 NaOH was simultaneously added into the aqueous solution under pH 10. The precipitation was aged at room temperature for a few hours for Cu^{2+}-Al^{3+} based hydrotalcite. The products were filtered with Buchner funnel. They were separated and sufficiently washed by deionized water and dried at 50 ℃ for 24 hours.

The products of Cu^{2+}-Al^{3+} based hydrotalcite were characterized with various methods. The local structures around Al for Cu^{2+}-Al^{3+} based hydrotalcite were evaluated by measuring X-ray adsorption near edge structure at BL2A in UVSOR with KTP.

For the comparison, Mg-Al hydrotalcite samples prepared by the co-precipitation method were similarly evaluated. Cu^{2+}-Al^{3+} based hydrotalcite samples synthesized by the co-precipitation method was powdered. the results of powder X-ray diffraction analysis showed that all samples for Cu^{2+}-Al^{3+} based hydrotalcite with different Cu^{2+}/Al^{3+} ratio of 2 to 4 were identified to be a layered double hydroxide. Figure 1 shows the results of XANES of Al-*K* edge for Cu^{2+}-Al^{3+} based hydrotalcite and the commercial Mg-Al hydrotalcite and Mg-Al hydrotalcite samples prepared by the co-precipitation method. The spectrum of Cu^{2+}-Al^{3+} based hydrotalcite products were similar to one of commercial Mg-Al hydrotalcites. The difference between the peak positions of P-*K* edge of Cu^{2+}-Al^{3+} based hydrotalcite with different Cu^{2+}/Al^{3+} ratio of 2 to 4 was confirmed by XANES This differences was caused by the content of Cu in hydrotalcite structures.

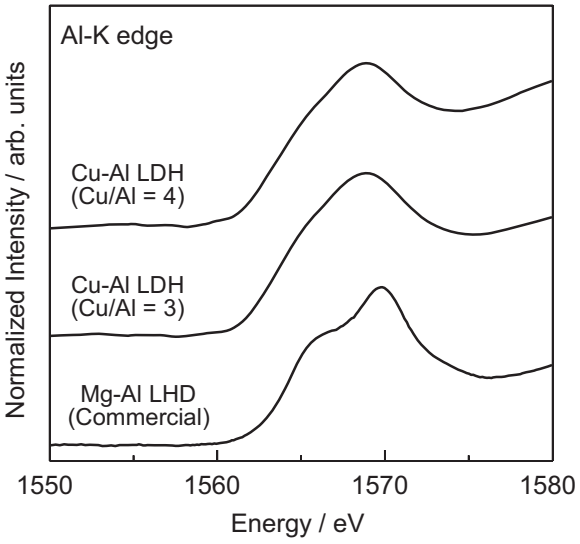

Fig. 1. Results of XANES of Al-*K* edge of the Cu^{2+}-Al^{3+} based hydrotalcite.

BL2A

Mo L_{III}-Edge XANES Study of Silylated Mo/H-MFI Catalysts for Methane Dehydroaromatization

H. Aritani[1], F. Ohya[1], K. Kuramochi[1], T. Sugawara[1], N. Naijo[1], K. Takanashi[1] and A. Nakahira[2]

[1]*Department of Life Science & Green Chemistry, Saitama Institute of Technology, Fukaya 369-0293, Japan*
[2]*Graduate School of Engineering, Osaka Prefecture University, Sakai 599-8531, Japan*

As a typical GTL (Gas-To-Liquid) catalyst in a direct conversion process of LNG, MoO_x-modified H-MFI zeolite (Mo/H-MFI) catalyst shows high activity for methane dehydroaromatization to produce benzene and naphthalene in the absence of oxygen. The important problem on the Mo/H-MFI catalysts is a rapid deactivation by coking and/or carbon contamination on the catalyst surface, and thus, highly active GTL catalysts with durable activity have been called for. Many workers have been revealed that reduction of Mo species is brought about in contact with methane in initial step. Reduced Mo ions tend to react methane to form carbide and/or oxycarbide species in next step [1]. The carbide species is active for methane dehydroaromatization, however, it is difficult to avoid the deactivation due to carbon deposition on the H-MFI surface. The carbon deposition proceeds mainly on the acid sites of H-MFI extraframework. On H-MFI interpores, appropriate acid sites shows durable activity with low deactivation rate. In the present study, silylated Mo/H-MFI catalysts were prepared in order to cover the acid sites of H-MFI extraframework. By silylation using organosilane regents, coking sites in extraframework can be covered selectively. In fact, the silylated Mo/H-MFI showed durable activity in the reaction with CH_4-H_2 at 973 K. To characterize the bare- and sylilated Mo-H-MFI catalysts, Mo L_{III}-edge XANES studies were applied. Red-ox states of the active Mo species on H-MFI with/without silylation were evaluated before/after the methane dehydroaromatization.

Catalysts were prepared by impregnation of H-MFI support with $MoO_2(acac)_2$–$CHCl_3$ solution, and followed by drying overnight and calcination at 773 K for 3 h. The amount of MoO_3-loading is 5.0 wt% in this study. H-MFI supports with Si/Al_2 = 20-72 were synthesized hydrothermally at 413 K for a week, and followed by ion-exchanging with NH_4Cl and calcination at 873 K. Silylation was carried out by impregnating triethoxyphenylsilane-heptane solution (Mo/Si=5) with Mo/H-MFI, and dried at 353 K for onernight. The catalytic activity of methane dehydroaromatization was evaluated by means of fixed bed flow reaction, as described in a separate paper [2]. Mo L_{III}-edge XANES spectra were measured in BL2A of UVSOR-IMS in a total-electron yield mode using InSb double-crystal monochromator. Photon energy was calibrated by using Mo metal-foil at Mo L_{III}-edge, and normalized XANES spectra and their second derivatives are presented. REX-2000 (Rigaku) software was used by normalization of each XANES spectrum.

Figure 1 shows the XANES spectra of bare- (shown in top) and silylated (in bottom) Mo/H-MFI catalysts (pretreated with CO(2%)-He) reacted with CH_4(20%)-He at various temperatures. Reduction of Mo species reflects the shift of lower edge energy. After reaction at 973-1023 K, Mo species on silylated Mo/H-MFI are reduced easier than that on bare one. At 1073 K, Mo^{2+} species due to Mo_2C are formed definitely in both catalysts. The silylated catalyst showed a maximum activity at 973 K, and thus, the silylation relates to the enhancement of Mo species to form partially carbonized (Mo-oxycarbonates, in major) ones. At the same time, carbon deposition was inhibited. These results suggest the inhibition of carbon coking and formation of active Mo species at lower temperature at 973K by silylation (Mo/Si=5).

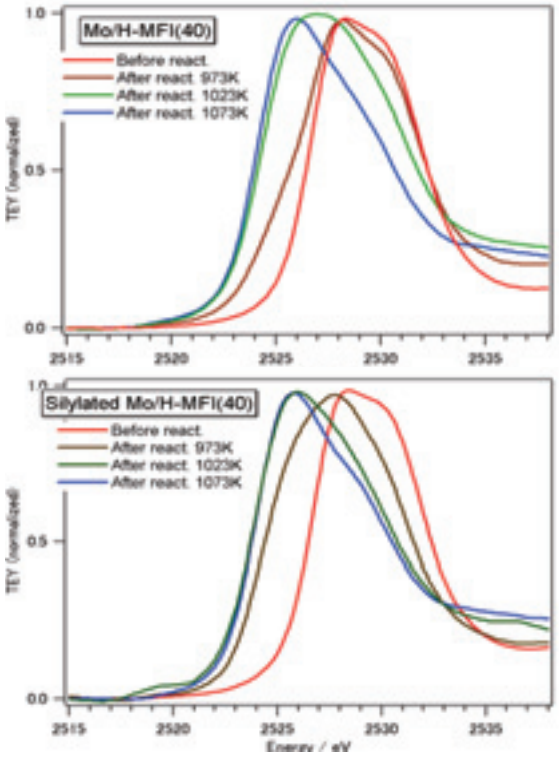

Fig. 1. Mo L_{III}-edge XANES of Mo/H-MFI (Si/Al_2=40) catalysts before and after silylation with phenylsilane (Mo/Si=5) reacted at various temperatures.

[1] H. Aritani, S. Shinohara, S. Koyama, K. Otsuki, T. Kubo and A. Nakahira, Chem. Lett. **35** (2006) 416.
[2] H. Aritani, H. Shibasaki, H. Orihara and A. Nakahira, J. Environm. Sci. **21** (2009) 736.

BL2A

Mg-*K* XANES Study of Mg-Doped Hydroxyapatite

H. Murata[1], K. Shitara[1], F. Oba[1] and I. Tanaka[1, 2]

[1]*Department of Materials Science and Engineering, Kyoto University, Kyoto 606-8501, Japan*
[2]*Nanostructures Research Laboratory, Japan Fine Ceramics Center, Nagoya 456-8587, Japan*

Hydroxyapatite (HAp) is a main inorganic component of human bones and teeth. HAp in human bodies contains various kinds of defects such as Ca vacancies, excess H and impurities. They affect biological properties of HAp [1] and thus it is important to understand their electronic and atomistic structures.

Mg is one of the essential elements for human bodies and a major impurity in human bones. It is considered to have an important role for bone re-modeling [1]. In this study, we investigated the local environments of Mg in HAp by Mg-*K* X-ray absorption near edge structure (XANES).

Undoped and Mg-doped HAp samples were synthesized using the solution-precipitation method. Starting materials were 0.1 mol/L solutions of $Ca(NO_3)_2{\cdot}4H_2O$, $Mg(NO_3)_2{\cdot}6H_2O$ and $(NH_4)_2HPO_4$. Precipitations were matured at 353 K for 5 hours in Ar atmosphere. Nominal Mg/(Ca+Mg) ratio was set to 0, 2, 5 and 20 at%. Mg-*K* XANES was measured at BL2A in UVSOR. The incident X-ray beam was monochromatized by beryl double crystals. XANES signals were collected with GaAsP photo-diodes (HAMAMATSU G-1127-02). Pellets of samples were mounted on carbon tapes. For a detailed analysis of Mg-*K* XANES, theoretical spectra were obtained by the first-principles supercell method with a core-hole effect [2].

Mg-doped HAp samples were characterized by XRD. No secondary phases were observed. The XRD patterns showed peak shifts and broadening by Mg doping. This indicated that Mg was incorporated into the HAp crystals.

The Mg-*K* XANES spectra of these samples were measured at BL2A. Usually, XANES signals in a soft X-ray region are collected by the total electron yield (TEY) method. However, our samples had a tendency to be charged up and we could not obtain high-quality spectra by the TEY method. Therefore, the fluorescent yield (FY) method with GaAsP photodiodes was employed. Figure 1 shows Mg-*K* XANES of the Mg-doped HAp samples measured by the FY method. The FY method gives good spectra for Mg with small concentrations.

It is found that the Mg-*K* XANES for 2, 5 and 20 at%Mg have the same features. In order to elucidate the local environments of Mg in HAp via the interpretation of Mg-*K* XANES, theoretical spectra were obtained. HAp has two non-equivalent Ca site, i.e., the Ca-1 (columnar) site and Ca-2 (triangular) site. We considered models in which one Mg was substituted for the Ca-1 or Ca-2 sites. However, neither model reproduced the experimental Mg-*K* XANES spectra. This indicated that Mg in HAp is not simply located at these sites. Our previous study suggested that the XANES of dopants in HAp is affected by association with the Ca vacancy and excess H [3]. Mg in HAp is likely to be associated with other defects as well. A detailed analysis of the defective structures is in progress.

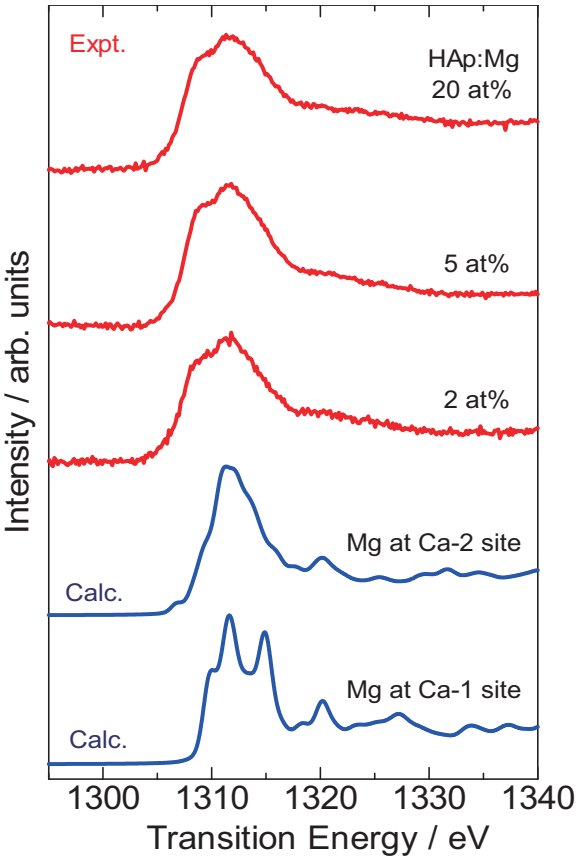

Fig. 1. Experimental and calculated Mg-*K* XANES of Mg-doped Hap.

[1] A. Boanini *et al.*, Acra Biomater. **6** (2009) 1882.
[2] I. Tanaka *et al.*, J. Am. Ceram. Soc. **88** (2005) 2013.
[3] H. Murata *et al.*, J. Phys.: Condens. Matter **22** (2010) 384213.

BL3U

Hybridized Electronic States near E_F of Potassium-Doped Picene Probed by Soft X-Ray Emission Spectroscopy

H. Yamane and N. Kosugi

Department of Photo-Molecular Science, Institute for Molecular Science, Okazaki 444-8585, Japan
School of Physical Sciences, The Graduate University for Advanced Studies, Okazaki 444-8585, Japan

Recently, a new organic superconductor has been discovered for a Potassium (K)-doped picene [see, Fig. 1(a)], with high transition temperatures (< 18 K), which depend on the K concentration [1]. In order to elucidate the nature of the superconductivity in the K-doped picene, detailed information on the electronic structure is required. It has been suggested from theoretical calculations that the dopant (K) orbitals are higher in energy and weakly hybridized with the molecular states close to the Fermi energy (E_F) [2]; however, experimental proofs for the formation of hybridized electronic states of the K-doped picene have not yet been reported.

In this work, in order to understand the local electronic structure of the K-doped picene, soft X-ray spectroscopies were applied at BL3U. The K-doped picene was prepared by the co-evaporation of picene (99.9% purity, NARD inst. Ltd) and K (SAES getters) on SiO_2/Si(111) at the fixed deposition rates with the post-annealing at 370 K. The K concentration and the crystallinity of the K_xPicene (x = 0, 3) were confirmed by CuKα X-ray diffraction (XRD) and fluorescence-yield X-ray absorption spectroscopy (FY-XAS).

Figure 1(a) shows the XRD scans of the K_xPicene (x = 0, 3), which agree well with the earlier study [1]. For the K-doped picene, the K atoms are intercalated in the stacked picene molecules.

Figure 1(b) shows FY-XAS spectra of the K_xPicene (x = 0, 3) at the normal incidence. The strong XAS peaks, originating from the C 1s → LUMO (π*) and LUMO+1 (π*) transitions [3,4], appear at the incident photon energy ($h\nu_{in}$) of 284–285 eV. These peaks are shifted to the lower $h\nu_{in}$ side and broadened upon the K doping due to the electron transfer from K 4s to LUMO and LUMO+1 of picene.

Figure 2 shows the selected soft X-ray emission (XES) spectra of the K_xPicene (x = 0, 3) at various $h\nu_{in}$. The elastic peak shows linear dispersion to the higher emission energy ($h\nu_{out}$) side with increasing $h\nu_{in}$. At $h\nu_{in}$ = 310.0 eV, the fluorescence feature in XES ($h\nu_{out}$ < 290 eV) for the K-doped picene shows a doping-induced peak near E_F at $h\nu_{out}$ = 288 eV very weakly, as indicated by the downed arrow, which is not observable for the undoped picene. From the $h\nu_{in}$ dependence of the XES spectra, we found that the doping-induced peak near E_F is pronounced after the K 2p excitation, $h\nu_{in} \geq$ 295 eV [see, Fig. 1(b) and 2].

These FY-XAS and XES results indicate that the molecular states of picene are hybridized with K 4s near E_F upon the K doping.

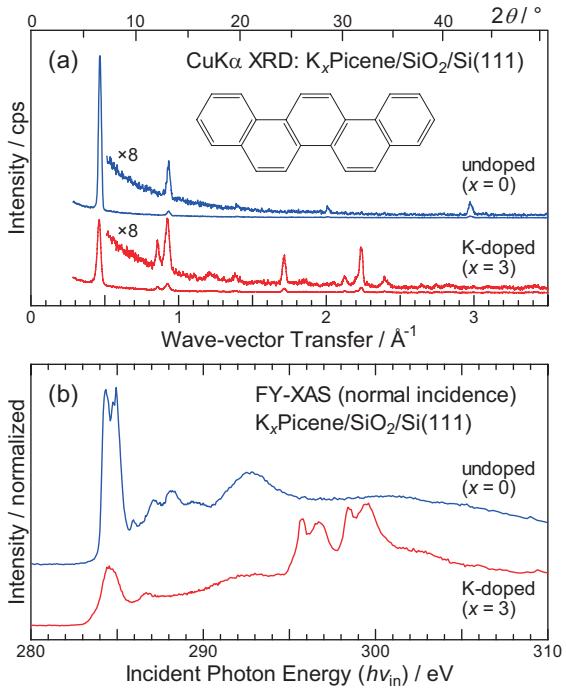

Fig. 1. (a) CuKα XRD and (b) FY-XAS spectra of K_xPicene (x = 0 and 3) films on SiO_2/Si(111).

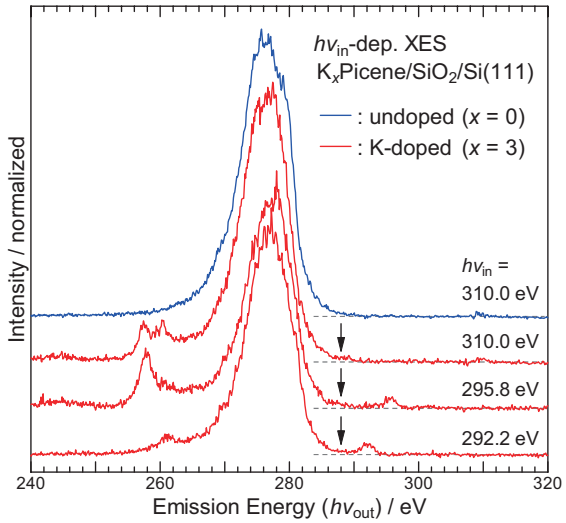

Fig. 2. XES spectra of K_xPicene (x = 0 and 3) films as a function of incident photon energy ($h\nu_{in}$).

[1] R. Mitsuhashi *et al.*, Nature **464** (2010) 76.
[2] G. Giovannetti and M. Capone, Phys. Rev. B **83** (2011) 134508.
[3] H. Ågren *et al.*, Chem. Phys. **196** (1995) 47.
[4] M. Obst *et al.*, Environ. Sci. Tech. **45** (2011) 7314.

BL3B

Optical Spectroscopy of ZnO:Al Thin Films

N. Kashiwagura, T. Hashida and T. Takeya
Department of Mathematical and Design Engineering, Gifu University, Gifu 501-1193, Japan

Today the most widely adopted TCO (transparent conductive oxides) films for use as electrodes of solar cell and liquid crystal display is ITO (Indium Tin Oxides) films. However, ITO films include so sparse Indium that the substitutive materials are expected. ZnO thin films are one of the hopeful materials as TCO films.

ZnO thin films were deposited on a fused silica glass (10 mm x 20 mm x 0.5 mm) by the DC sputtering method. The induced electric power, the substrate temperature were 12 W, 200 ℃, respectively, for all samples in common. The sputtering gas (Ar) pressure was 0.125, 0.2 and 0.3 Torr. for sample 1, sample 3 and sample 5, respectively.

Optical absorption, luminescence and excitation spectra were measured using the BL3B beam in the temperature range of 8-300 K.

Figure 1 shows the optical absorption spectra for ZnO thin films. The sharp edge at 150 nm (8.3 eV) for sample 1 is due to the absorption of fused silica substrate. The several broad bands below 360 nm (3.3 eV) are due to the band-to-band transition of ZnO. All the samples are efficiently transparent as TCO thin film above 380 nm (visible light region).

Figure 2 shows the luminescence spectra with various excitation wavelengths in sample 1 at 300 K. The band-to-band excitation below 360 nm produces several broad luminescence bands at 405 nm, at 425 nm and at 440-490 nm. In these spectra, the additional peaks around 540 and 590 nm are the influence from outer ceiling lights, which could not be perfectly eliminated. As the excitation wavelength increases (the excitation energy decreases), the intensity of luminescence bands decreases as a whole.

Figure 3 shows the luminescence spectra in sample 5 at 300 K. The spectra exhibit several broad luminescence bands at 405 nm, at 425 nm and at 440-490 nm. The spectra are very similar to that of sample 1. With increasing the excitation wavelength, the luminescence intensities decrease as a whole.

The band around 425 nm is estimated to be intrinsic luminescence (for example, self-trapped exciton). The broader band around 470 nm is estimated to be the luminescence associated with defects (for example, donor/acceptor recombination).

The relation between the luminescence and electrical conductivity will be examined. In this study, optical properties of Al doped ZnO thin films were investigated. It seems to be important to investigate the exact Al concentration in thin films which are made by sputtering with the target including 2% Al nominally.

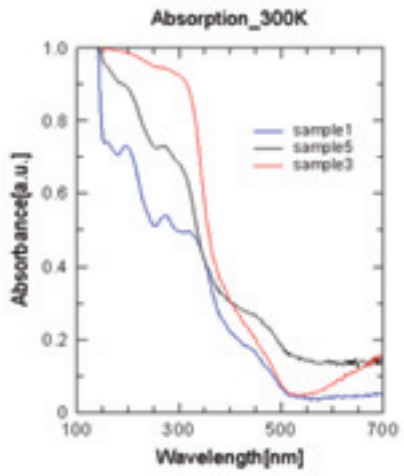

Fig. 1. Absorption spectra in ZnO thin films at 300 K.

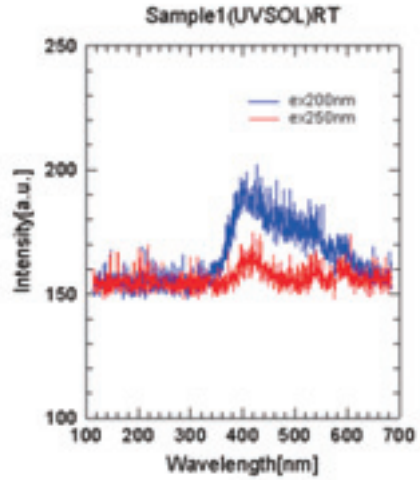

Fig. 2. Luminescence spectra in sample 1 at 300 K.

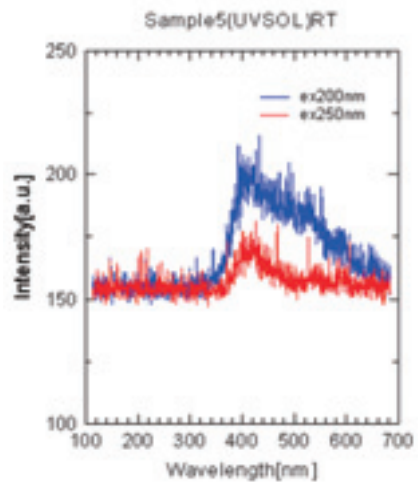

Fig. 3. Luminescence spectra in sample 5 at 300 K.

BL3B

Optical Spectroscopy of $Cd_{1-x}Mn_xTe$ Crystals

M. Yamaga, Y. Ogoshi, A. Kanetake, S. Takano, T. Nohisa, S. Tsuda and H. Tsuzuki
Department of Material and Design Engineering, Gifu University, Gifu 501-1193 Japan

$Cd_{1-x}Mn_xTe$ crystals have magneto-optical properties induced by Mn^{2+} ions. They are very useful as applications to an optical isolator.

In a previous activity report [1], optical properties of $Cd_{1-x}Mn_xTe$ crystals (x=0.5) were reported. In this report, the composition x is extended from 0.1 to 0.9 in the whole range of the composition. $Cd_{1-x}Mn_xTe$ crystals were grown by the vertical Bridgeman method. The compositions, x, of the crystals are 0.1, 0.25, 0.3, 0.5, 0.75, 0.9 being equal to the melting compositions [2].

Figure 1 shows the absorption spectra observed in $Cd_{1-x}Mn_xTe$ (x=0.1, 0.25, 0.3, 0.5, 0.75, 0.9) at 300 K. The band gap energy related to the absorption edge of the crystal increases with an increase of x up to 0.5 and slightly decreases above 0.6. This result suggests that the phase transition of the crystal $Cd_{1-x}Mn_xTe$ occurs around x=0.6 from zinc blende to hexagonal phases. The sample temperature is decreased from 300 K, the band edge is shifted to the short wavelength, resulting in the large band gap.

Figure 2 shows temperature dependence of the luminescence spectra for $Cd_{0.9}Mn_{0.1}Te$. The peak of the luminescence is around 720 nm and just below the band edge energy observed at 20 K. The luminescence peak is shifted to the longer wavelength and the intensity markedly decreases with an increase of temperature. The intensity is negligibly small above 140 K. In the same way, Fig. 3 shows the luminescence spectra of $Cd_{0.25}Mn_{0.75}Te$ at various temperatures. The luminescence peak is shifted to the short wavelength compared with that for $Cd_{0.9}Mn_{0.1}Te$. However, the line width for $Cd_{0.25}Mn_{0.75}Te$ is the largest for all crystals with the compositions of x=0.1, 0.25, 0.3, 0.5, 0.75, 0.9.

We consider the origin of the luminescence from $Cd_{1-x}Mn_xTe$ (x=0.1, 0.25, 0.3, 0.5, 0.75, 0.9) crystals. The luminescence may be assigned to weakly localized excitons. The line width has the maximum for x=0.75. This result is consistent with the ESR results of Mn^{2+} in $Cd_{1-x}Mn_xTe$ (x=0.1, 0.25, 0.3, 0.5, 0.75, 0.9) that the ESR line width has also the maximum at x=0.75. The line broadening is due to local magnetic field created by Mn^{2+} cluster in the $Cd_{1-x}Mn_xTe$ crystals.

[1] M. Yamaga, UVSOR Activity Report **38** (2010) 117.
[2] M. Prakasam, O. Viraphong, L. Teule-Gay, R. Decourt, P. Veber, E. G. Villora and K. Shimamura, J. Crystal Growth **318** (2011) 533.

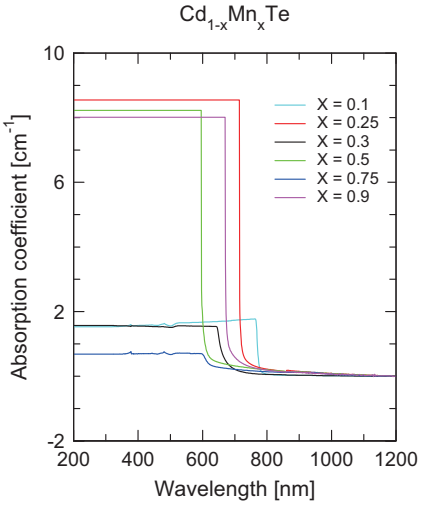

Fig. 1. Absorption spectra of $Cd_{1-x}Mn_xTe$.

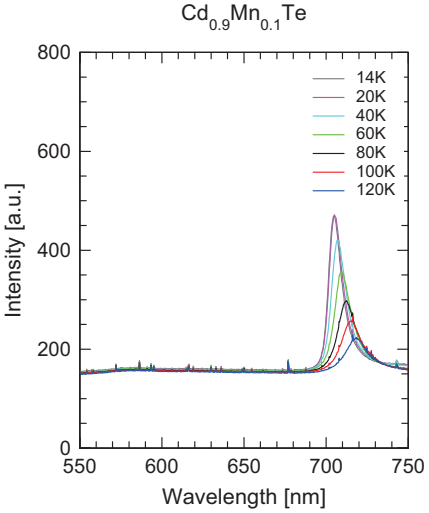

Fig. 2. Luminescence spectra in $Cd_{0.9}Mn_{0.1}Te$.

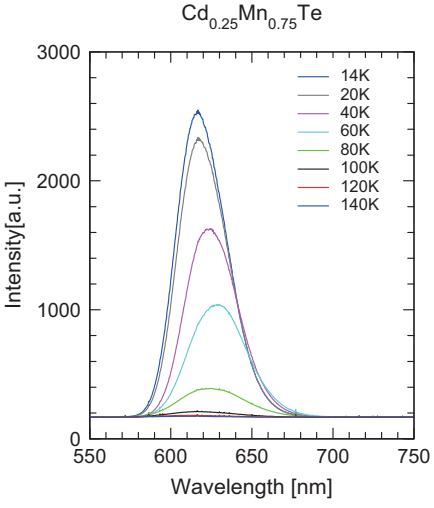

Fig. 3. Luminescence spectra in $Cd_{0.25}Mn_{0.75}Te$.

BL4B

Annealing Effect on Local Structure of Diamond-Like Carbon and Tungsten-containing Diamond-Like Carbon Films

A. Fujimoto and K. Kanda

Laboratory of Advanced Science and Technology for Industry, University of Hyogo Kamigori, Ako, Hyogo 678-1205, Japan

Diamond-like carbon (DLC) film is expected to use as various industrial fields, because of its some excellent properties such as hard, low friction coefficient, low surface energy and so on. Recently, incorporation of Tungsten (W) into DLC films was proposed because it was known that this incorporation improved the film's thermal durability. In the present study, the effect of annealing on DLC and tungsten containing DLC (W-DLC) films in vacuum was investigated from the measurement of the annealing temperature dependence on the carbon K-edge near-edge x-ray absorption fine structure (NEXAFS) spectra of the commercial DLC and W-DLC films fabricated by various methods for industrial use.

Sample commercial DLC and W-DLC films were prepared on the Si substrate with ≈200 nm film thickness using several deposition methods: 1) DLC and W-DLC films by unbalanced magnetron sputtering (UBMS) (KOBELCO Co., Ltd.), 2) DLC film fabricated by ion plating (IP) (NANOTEC Co., Ltd.), 3) DLC film fabricated by plasma-enhanced CVD (PE-CVD) (Nippon-ITF Inc.). These samples were annealed in a furnace (Thermo RIKO Co. Ltd; GFA430) under vacuum conditions ($<10^{-4}$ Pa). The annealing temperature was 673, 773, or 873 K, and the annealing time was 32 h. C-K NEXAFS spectra were measured at the BL4B of UVSOR and BL09A of NewSUBARU. The NEXAFS spectra were measured in the energy range 275-320 eV with 0.5 eV FWHM resolution in the total electron yield mode.

In the C-K NEXAFS spectra of DLC films, sharp peak, which is assignable to the transitisons from the C 1s level to the unoccupied π* levels of the sp^2 (C=C) and/or sp (C≡C) sites, is observed at 285.4 eV. The intensity of this peak increased with the annealing temperature, which indicated the increase of sp^2 ratio in the film. The procedure used to estimate the $sp^2/(sp^2+sp^3)$ ratio is described elsewhere [1]. Figure 1 shows the dependence of the $sp^2/(sp^2+sp^3)$ ratios of the films on the annealing temperature. The $sp^2/(sp^2+sp^3)$ ratios of the commercial W-DLC and DLC films as deposited were estimated to be 0.3-0.4. The $sp^2/(sp^2+sp^3)$ ratios of all the W-DLC and DLC films increased with the annealing temperature indicating that a graphite structure had formed[2]. Therefore, the onset of increase in $sp^2/(sp^2+sp^3)$ ratio was positioned at higher temperature indicated that the film had strong thermal durability. In short, thermal durability of these films was stronger in the order of IP DLC, UBMS W-DLC, UBMS DLC, and PE-CVD DLC films

As a result, the present study confirmed following facts from local structure level by the measurement of NEXAFS spectra: 1) Thermal stability of DLC films was varied on the deposition method of film. 2) Incorporation of W improves the film's thermal durability.

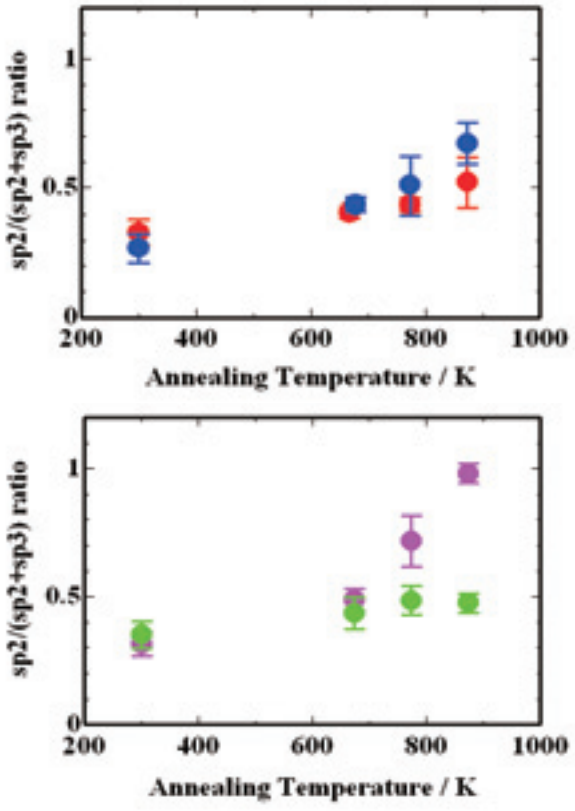

Fig. 1. Dependence on annealing temperature of $sp^2/(sp^2+sp^3)$ ratio:. a): UBMS W-DLC and : UBMS DLC films;. b): PE-CVD DLC and : IP DLC films. Points at 273 K indicate $sp^2/(sp^2+sp^3)$ ratio as deposited.

[1] K. Kanda, T. Kitagawa, Y. Shimizugawa, Y. Haruyama, S. Matsui, M. Terasawa, H. Tsubakino, I. Yamada, T. Gejo and M. Kamada, Jpn. J. Appl. Phys. **41** (2002) 4295.

[2] K. Kanda, J. Igaki, N. Yamada, R. Kometani and S. Matsui, Diamond Relat. Mater. **18** (2009) 490.

BL4B

Electronic Structural Changes of $LiNi_{0.5}Mn_{1.5}O_4$ during Lithium-Ion Intercalation/Deintercalation

T. Okumura, M. Shikano and H. Kobayashi

Research Institute for Ubiquitous Energy, National Institute of Advanced Industrial Science and Technology (AIST), Midorigaoka 1-8-31, Ikeda, Osaka 563-8577, Japan

Lithium-ion batteries (LIB) with high energy density, safety, and durability are required for electric vehicles (EV), hybrid electric vehicles (HEV), and plug-in hybrid electric vehicles (PHEV) as their power sources. Lithium nickel manganese spinel oxide $LiNi_{0.5}Mn_{1.5}O_4$ is one of the candidates for the positive electrode materials for LIBs as an alternative to the conventional $LiCoO_2$ cathode because of its low cost and low toxicity[1]. Moreover, its specific capacity above 4.5 V is suitable for designing the next-generation LIB with the high energy density. In order to get the guide to improve the superior electrochemical properties, understanding the detailed electronic structural changes in $Li_xNi_{0.5}Mn_{1.5}O_4$ during lithium-ion intercalation/deintercalation process is essential as reported in other electrode materials[2].

The $Li_xNi_{0.5}Mn_{1.5}O_4$ samples with various lithium concentrations have been picked up from the batteries after intercalation or deintercalation as shown in Fig. 1. Ni L_3-edge, Mn L_3-edge and O K-edge XANES spectra were measured with total electron yield mode. The Ni and Mn L_3-edge spectra at various lithium contents (shown in Fig. 2 (a) and (b), respectively) correspond to the electronic transitions from the $2p_{3/2}$ states to an unoccupied 3d state. At $x < 1$, the absorption edge peak at the right shoulder of Ni L_3-edge peaks clearly appeared with the decrement of the lithium-ion contents although the significant change could not be observed in Mn L_3-edge peaks. This result indicates that the charge variation during lithium-ion deintercalation was compensated by the redox reaction of the Ni^{2+}/Ni^{4+} couple[3]. On the other hand, at $x > 1$, the absorption edge energy of Mn L_3-edge peaks shifted towards lower energy levels with an increase of lithium content while Ni L_3-edge peaks were mostly maintained. This result indicates that the charge variation during lithium-ion intercalation was compensated by the redox reaction of the Mn^{3+}/Mn^{4+} couple [3]. The large voltage gap between $x < 1$ and $x > 1$ in Fig. 1 results from the difference of the redox-ion species.

The O K-edge spectra were shown in Fig. 2 (c). The absorption edge peaks appeared around 528-535 eV particularly indicate the transition from O 1s to hybridized orbital of O 2p with transition-metal 3d[2]. At $x > 1$, the shape of the peaks changed with the increase of the lithium content as well as the shape of Mn L_3-edge peaks changes as written above, although it maintained at $x > 1$.

These results indicated that both manganese and oxide ions contributed on the redox reaction at $x < 1$, and the only nickel ion affect the redox reaction at $x > 1$. Thus, the electronic structural change of oxide ion is also crucial for considering redox reaction at charging/discharging batteries, and the contribution of the oxide ion on redox reaction differs in various redox cation species.

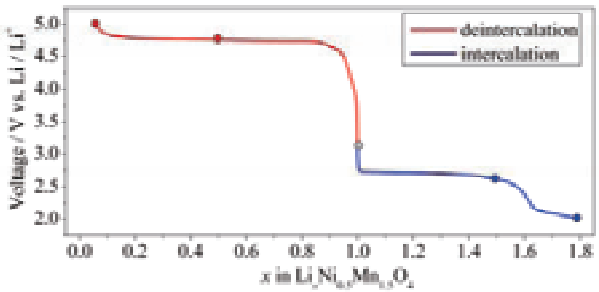

Fig. 1. Lithium-ion intercalation/deintercalation behavior in $LiNi_{0.5}Mn_{1.5}O_4$ spinel oxide. Circles indicate lithium content of samples measured XANES spectra.

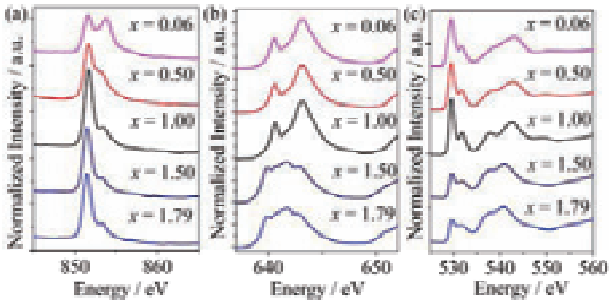

Fig. 2. XANES spectra of Ni L_3-edges (a), Mn L_3-edges (b), and O K-edges (c) in $Li_xNi_{0.5}Mn_{1.5}O_4$.

[1] Q. Zhong *et al.*, J. Electrochem. Soc. **144** (1997) 205.
[2] *for example*, T. Okumura *et al.*, Dalton Trans. **40** (2011) 9752.
[3] Y. Terada *et al.*, J. Solid State Chem. **156** (2001) 286.

BL5U

Valence-Band Electronic Structure of N-Implanted TiO_2

K. Soda[1], T. Owada[2], K. Morita[2], S. Harada[1], E. Kuda[1] and T. Yoshida[3,1]

[1]*Graduate School of Engineering, Nagoya University, Nagoya 464-8603, Japan*

[2]*Department of Physical Science and Engineering, Nagoya University, Nagoya 464-8603, Japan*

[3]*EcoTopia Science Institute, Nagoya University, Nagoya 464-8603, Japan*

TiO_2 is well-known as a photocatalyst with a band gap of ~3 eV [1]. Recently, Yoshida *et al*. have found that TiO_2 gains the photoactivity for visible light by N^+ ion implantation and that N occupying at the O site is responsible for the visible-light activity by the N *K*-edge near-edge X-ray absorption fine structure (NEXAFS) measurement [2]. In this study, we have investigated valence electronic structure of such N^+ implanted TiO_2 to clarify the origin of the visible-light photoactivity.

Photoelectron measurement were carried out at room temperature in the angle-integrated mode with total energy resolution of ~0.1 eV. Specimens were rutile TiO_2 (100) plates, which were first *in situ* cleaned by 5-keV Ar^+ ion sputtering and then implanted with 5-keV N^+ or N_2^+ ions. The origin of the binding energy E_B was set to the Fermi energy E_F of a gold plate on a sample holder.

Figure 1 shows typical photoelectron spectra recorded before and after the N^+ implantation with the excitation photon energy $h\nu$. In the figure, the background due to the secondary electrons are subtracted from the measured spectra and their intensity is normalized with the integrated intensity from E_F up to E_B = 12 eV. In the upper panel, spectra after the Ar^+ sputtering and subsequent N^+ implantation of ~8 x 10^{20} ions m^{-2} are compared by shifting the spectrum after the implantation towards the high binding energy side so that the valence band bottom (E_B = 8 ~ 9 eV) may coincide with each other. The N *K*-edge NEXAFS measurement for this sample confirms the formation of visible-light active N species. After the sputtering, a broad hump appears in the upper part of the gap around E_F. This is due to the reduction of Ti or defect formation, induced by the sputtering, which also leads to the increase in electrons in the Ti 3*d* conduction band. Observed apparent shift of the Fermi edge towards the high binding energy side after the implantation implies the decrease in defects and conduction electrons, which may be caused by the recovery of the chemical bond, *i.e.* new Ti-N bond formation. Spectral increase due to the N 2*p* states derived from the Ti-N bond appears in the upper part of the O 2*p* valence band and in the lower region of the gap (E_B = 3 ~ 6 eV). The assignment of these new bands after the implantation is also confirmed by the Ti 3*p*-3*d* resonance behavior around $h\nu$ = 50 eV, which is shown in the lower panel of the figure for the spectra after the implantation. At $h\nu$ = 50 eV, the hump around 0.5 eV, Ti 3*d* conduction band or defect states, and the O 2*p*-Ti 3*d* bonding valence band at E_B ~ 7 eV are enhanced due to the resonance photoemission of the Ti3*d* electrons [3], while the states at E_B = 3 ~ 6 eV show no prominent increase, because they are mainly derived from O 2*p* and N 2*p* states. These are consistent with a band calculation for TiO_2 and N-substituted $TiO_{2-x}N_x$ [1].

Similar results have already reported by Batzill *et al*., who concluded that the impurity states just above the valence band without the band-gap narrowing were formed by N doping [3]. However, the present results together with the NEXAFS ones suggest that the implanted N occupies the O site and forms a common valence band extending into the band gap in the surface region; the top of the valence band is located at E_B ~ 2.5 eV, which is comparable with reported threshold of the photoactivity in the decomposition of methylene blue for the N-doped TiO_2 [1]. The Ti 3*d* defect states just below the conduction band also induce visible-light absorption but are not responsible for the photoactivity.

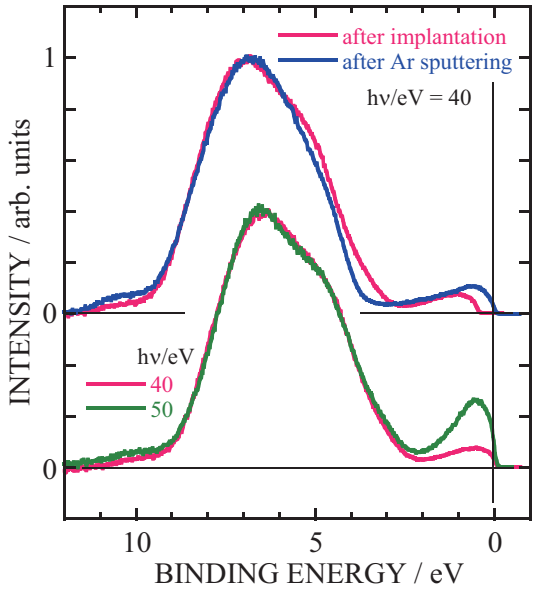

Fig. 1. Valence-band spectra of N-implanted TiO_2.

[1] R. Asahi *et al.*, Science **293** (2001) 269.
[2] T. Yoshida *et al.*, Mater. Sci. Forum **561-565** (2007) 567.
[3] M. Batzill *et al.*, Phys. Rev. Lett. **96** (2006) 026103.

BL5U

Effects of Periodicity Imperfection on Mini-Bands in Semiconductor Superlattice

K. Hashimoto[1], D. Shimura[1], M. Kuwahara[2], S. Harada[1], T. Ujihara[1], M. Matsunami[3] and S. Kimura[3]

[1]*Graduate School of Engineering, Nagoya University, Nagoya 464-8603, Japan*
[2]*EcoTopia Science Institute, Nagoya University, Nagoya 464-8603, Japan*
[3]*UVSOR Facility, Institute for Molecular Science, Okazaki 444-8585, Japan*

Recently a highly-optimized intermediate band solar cell, of which a high conversion efficiency can reach 74.6% theoretically, is proposed [1]. The concept is to utilize intermediate bands in the carrier excitation in order that the band structure is adjusted to the solar light spectrum. As intermediate bands, the mini-band due to a periodic quantum structure (superlattice structure) is used. But there is a problem that it is presently impossible to produce quantum dots of equal size and perfect periodicity.

In this study, the effects of periodicity imperfection on the mini-band structure, especially hole mini-bands, were investigated. We examined a superlattice structure which consists of multiple quantum wells because the preparation method has been established.

Figure 1 shows the detailed structures of each sample: A GaAs bulk sample, a periodic superlattice and a disordered superlattice of which second well layer was made thinner. Amorphous arsenic layers were deposited on the sample surfaces to suppress oxidation, and they were removed just before the measurements by heat-treatment. On the evaluation of the mini-band structure, the synchrotron-radiation photoemission measurements were performed at BL5U of the UVSOR facility.

Figure 2 shows the electron density mappings in a valence band around Γ point. The red dots and green dots indicate the band structure determined from the peak values of the second order differential. They are a heavy hole band and a light hole band, respectively. In the case of bulk GaAs, the band structures are quadric curves. In addition, they are doubly-degenerated at $k_z = 0$. On the other hand, the band structures of the periodic superlattice and the disordered superlattice are not degenerated at $k_z = 0$. Moreover, they are also folded symmetrically on the white arrows, which indicate the interval of the Brillouin zone due to the periodic structure of superlattice. Therefore, their band structures are mini-bands.

The mini-band structures are characterized by the width of band splitting between the heavy hole mini-band and the light hole mini-band. Figure 3 shows the width of band splitting as a function of the wavenumber. The width of the disordered superlattice is wider than that of of the periodic superlattice. This is attributed to the following discussion: Due to the thinner well, the heavy hole band and the light hole band of the disordered superlattice were lower than those of the periodic superlattice. The band shift amount of the light hole band is larger than that of the heavy hole band by a difference in the effective mass. As a result, the width of the disordered superlattice is wider.

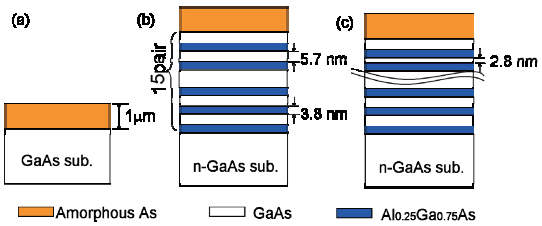

Fig. 1. Schematic images of the sample structure. (a) GaAs, (b) periodic superlattice and (c) disordered superlattice.

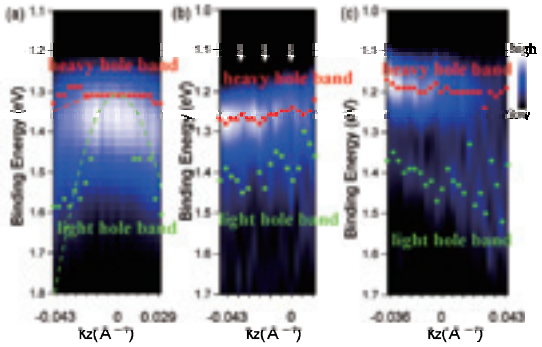

Fig. 2. Electron density mappings of (a) GaAs, (b) periodic superlattice and (c) disordered superlattice.

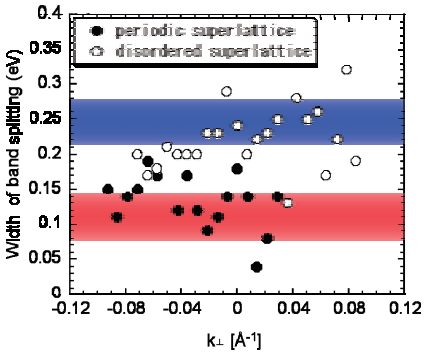

Fig. 3. Width of band splitting between heavy hole mini-band and light hole mini-band.

[1] T. Nozawa and Y. Arakawa, Appl. Phys. Lett. **98** (2012) 171108.

BL5B

Photodegradation in Amorphous Chalcogenide Semiconductor Films by Vacuum Ultraviolet Absorption Spectroscopy

K. Hayashi

Department of Electrical and Electronic Engineering, Gifu University, Gifu 501-1193, Japan

It is well known that amorphous chalcogenide semiconductor materials show a variety of photoinduced effects [1-4]. The prominent photoinduced phenomenon in these materials is a time-dependent decrease in photocurrent during and after irradiation of bandgap (BG) light [3,4]. This phenomenon is usually called photodegradation and is explained in terms of light-induced metastable defects (LIMD). In the device application of these materials, LIMD creation is a serious problem. Although a number of models have been proposed for LIMD creation [4], details of the mechanism underlying LIMD creation in these materials are still not clear. Understanding the physical mechanism underlying metastability is one of the important fundamental problems related to these materials.

Recently, I found a new phenomenon that photocurrent by irradiation of BG light increased in amorphous chalcogenide films. This phenomenon is not explained in terms of LIMD creation. These photoinduced phenomena can in general be either irreversible, i.e. the photoinduced changes are permanent after irradiation, or reversible, in which case the changes can be removed by annealing to the glass-transition temperature. The new phenomenon was an irreversible change. The photoinduced changes by BG light of the x-ray diffraction and the volume have directly shown that these phenomena are due to a change of the local structure of the amorphous network. However, several previous studies of photoinduced phenomena have reported that there is no direct correlation among photodegradation, photodarkening and photoinduced volume change.

Our recent studies have focused on the photoinduced energy structure changes in the vacuum ultraviolet (VUV) region by irradiation of BG light. Few studies have examined whether the photoinduced change of the chemical bonds contributes to photodegradation and photodarkening. To understand the dynamics and the correlation of photoinduced structure changes in the VUV region and the photoinduced change of photocurrent in amorphous chalcogenide semiconductors, real time in-situ measurements are required. In previous report, those dynamics and correlations are examined by measuring the total photoelectron yield (TPEY) that can measure the optical property in the VUV region. However, the beam position, brightness, and the energy stability were insufficient in the observation of the dynamics of TPEY by irradiation of BG light in UVSOR. In this report, I will discuss the stability of light source.

Samples used for the measurement of the transmission spectrum were amorphous chalcogenide (a-As_2S_3 and a-As_2Se_3) semiconductor thin films prepared onto aluminum thin films. Typical thickness of the sample and the aluminum films were around 200nm and 100nm respectively. The aluminum film was also used in order to eliminate the higher order light from the monochromator in the VUV region. The measurements were performed at room temperature. A pinhole of 1.5mm in a diameter was inserted between the monochromator and sample to remove stray light. The intensity of the VUV light was monitored by measuring the TPEY of a gold mesh.

Figure 1 shows the spectra of the light source under the same condition monitored by measuring the TPEY of a gold mesh. As shown in the figure, the spectrum reproducibility in the top-up operation is not good. We are examining the method to increase the accuracy of measurement at present.

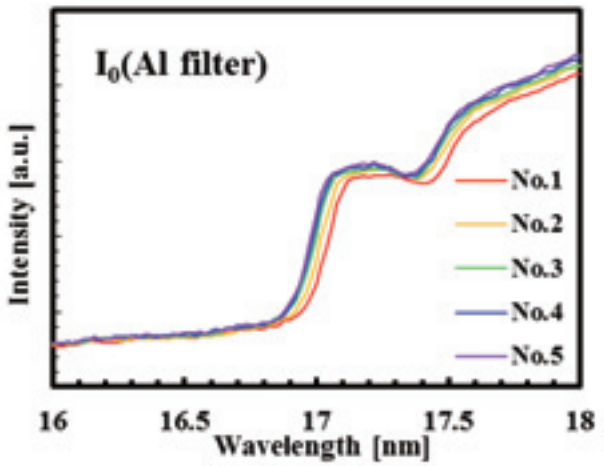

Fig.1. Spectra of the light source under the same condition monitored by measuring the TPEY of a gold mesh.

[1] K. Tanaka, Rev. Solid State Sci. **4** (1990) 641.
[2] S. R. Elliot, J. Non-Cryst. Sol. **81** (1986) 71.
[3] D. L.Staebler and C. R. Wronski, Appl. Phys. Lett. **31** (1977) 292.
[4] K. Shimakawa, A. Kolobov and S. R. Elliott, Adv. Phys. **44** (1995) 475.

BL6U

Extended Electronic States in Crystalline Guanine-Cytosine Watson-Crick Multilayers

R. Friedlein[1], Y. Wang[1], H. Yamane[2] and N. Kosugi[2]

[1] *School of Materials Science, Japan Advanced Institute of Science and Technology, Ishikawa 923-1292, Japan*

[2] *Dept. of Photo-Molecular Science, Institute for Molecular Science, Okazaki 444-8585, Japan*

In order to elucidate the role of intermolecular interactions in the pre-biotic assembly of RNA precursor oligomers, it is crucial to understand, if and in which way one-dimensional, stacked assemblies of Watson-Crick (WC) pairs may be formed without the presence of a backbone. With scanning tunneling microscopy studies limited to monolayer assemblies [1], the nature of the stacking between individual nucleic acids as well as of WC pairs has so far only been studied theoretically [2].

In recent home-based experiments we have found that the two nucleic acids guanine and cytosine assemble into an ordered multilayer film based on the hydrogen bonding within WC pairs (Fig. 1). The stability of WC pairs is high such that a macroscopic phase separation does not occur. Thin mixed films, about 2-3 nm thick, have been prepared under ultra-high vacuum conditions by co-deposition of guanine and cytosine molecules, at equal rates with respect to the amount of molecules, on the surface of highly-oriented pyrolytic graphite, HOPG(0001), held at 25 °C. The samples have then been exposed to water vapor *in situ*, and transferred in air to the experimental set-up at BL6U of the UVSOR facility.

Photon-energy dependent valence band photoelectron spectra obtained in the normal emission direction are shown in Fig. 1. The onset of the spectra is related to the highest occupied molecular orbital (HOMO) of guanine. It shows a clear dispersion with the photon energy which is consistent with the formation of extended electronic states related to the guanine HOMO similar to those in guanine multilayer films [3]. This demonstrates a quasi-columnar arrangement of the guanine molecules oriented in the direction normal to the surface and an anti-parallel stacking with two molecules per repeat unit along the stacks. Non-dispersing states at higher binding energy, denoted “A” and “B”, are related to cytosine molecules that have a significantly smaller intermolecular π-π overlap.

In order to accomplish an anti-parallel stacking in a layered arrangement, subsequent WC pairs must be flipped with respect to each other. As verified by quantum-chemical calculations [4], in this configuration, the cytosine molecules stack with those from neighboring WC pairs. This is in stark contrast to the arrangement realized in RNA which indicates an important role of the backbone sugars in preventing otherwise preferred anti-parallel stacking configurations.

Financial support from the SHIBUYA and MARUBUN Foundations is acknowledged.

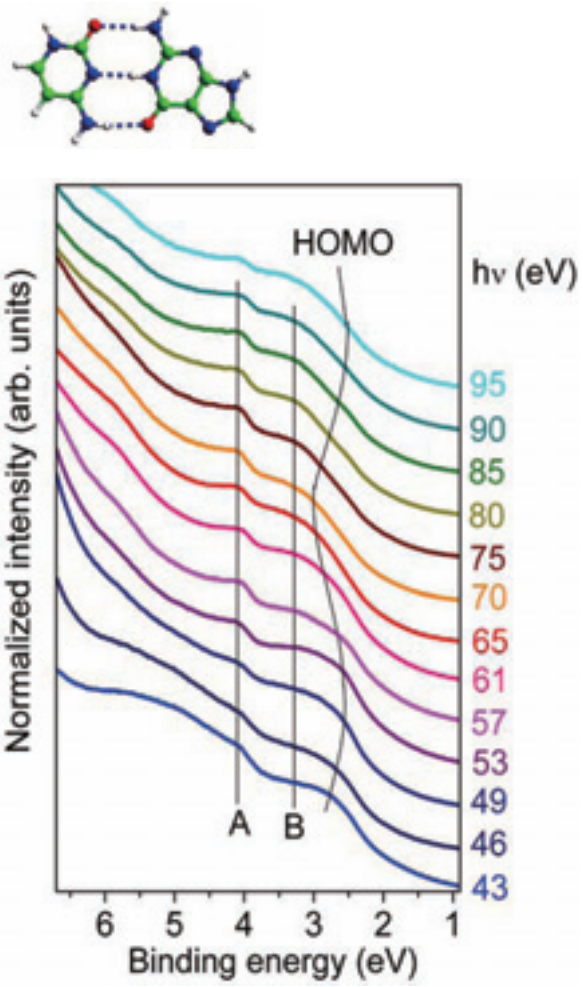

Fig. 1. The structure of a cytosine-guanine WC pair (top), and photon-energy-dependent photoelectron spectra of the mixed film (bottom). The dispersion of the guanine-derived HOMO is indicated by a solid line.

[1] S. Xu, M. Dong, E. Rauls, R. Otero, T. R. Linderoth and F. Besenbacher, Nano Lett. **6** (2006) 1434.

[2] C. Acosta-Silva, V. Branchadell, J. Bertran and A. Olivia, J. Phys. Chem. B **114** (2010) 10217.

[3] R. Friedlein, Y. Wang, A. Fleurence, F. Bussolotti, Y. Ogata and Y. Yamada-Takamura, J. Am. Chem. Soc. **132** (2010) 12808.

[4] Y. Wang, F. Negri, H. Yamane, N. Kosugi and R. Friedlein, in preparation.

BL6U

Band Alignment at CNT/n-Type 4H-SiC Interface Formed by Surface Decomposition of SiC

T. Maruyama[1], S. Sakakibara[1], Y. Ishiguro[1], H. Yamane[2] and N. Kosugi[2]
[1]*Department of Materials Science and Engineering, Meijo University, Nagoya 468-8502, Japan*
[2]*Institute for Molecular Science, Okazaki 444-8585 Japan*

Carbon nanotube (CNT) growth by surface decomposition of SiC is a synthesis method for self-organized CNT films only by heating SiC(000-1) carbon-face in a high vacuum [1]. By this method, high-density, well-aligned zigzag-type CNTs can be produced perpendicular to the substrate surfaces. In addition, CNTs were atomically bonded to SiC without any interlayers [2]. Previously, we reported both electrical property and electronic structure for CNT/n-type 6H-SiC and showed the presence of Schottky barrier at the interface [3]. In this study, we performed photoemission spectroscopy (PES) experiments for CNT/n-type 4H-SiC interface and determined the band alignment.

CNT films formed by surface decomposition of n-type 4H-SiC(000-1) were used as samples. For PES measurements, we prepared three kinds of samples with different CNT thicknesses; CNTs (~300 nm) on 4H-SiC, CNTs (several nm) on 4H-SiC and 4H-SiC(000-1) substrate. The PES measurements were carried out in a high-resolution angle-resolved PES system at BL6U. All PES spectra were measured at normal emission with the incident photon energy of 60 and 350 eV. The overall energy resolution was below 100 meV at room temperature (~300K).

Figure 1 (a) shows PES spectrum near valence band maximum (VBM) of CNTs (~300 nm) formed on 4H-SiC with that of Au. The Fermi edge is observed in the spectrum of CNTs, confirming that they were metallic, as reported for CNT films on 6H-SiC [3]. The band alignment at the CNT/SiC interface can be evaluated by measuring the binding energy of C 1s core level at the CNT/4H-SiC interface, the energy separation between the VBM and the C 1s core level of 4H-SiC and that between the Fermi edge and the C 1s level of CNTs [3]. Figure 1 (b) shows PES spectrum of the C 1s core level of CNT/SiC interface. By peak fitting, the energy separation in the C 1s core level between CNT and 4H-SiC was estimated to be 1.36 eV. From the PES measurements, we also determined the binding energy of C 1s peaks of CNTs (~300 nm) to be 284.35 eV and the energy separation between the VBM and C 1s core level of SiC to be 279.30 eV.

From these values, the band alignment at the CNT/4H-SiC interface was obtained, which is shown in Fig. 2. It should be noted that, in contrast with the CNT/n-type 6H-SiC interface, Schottky barrier was not formed at the CNT/4H-SiC interface. This result is consistent with recent experimental results about the current-voltage (I-V) characteristics of CNT(~300 nm)/n-type 4H-SiC heterojunction, which showed Ohmic behavior [4].

This work was supported in part by the Joint Studies Program (2011) of the Institute for Molecular Science (IMS).

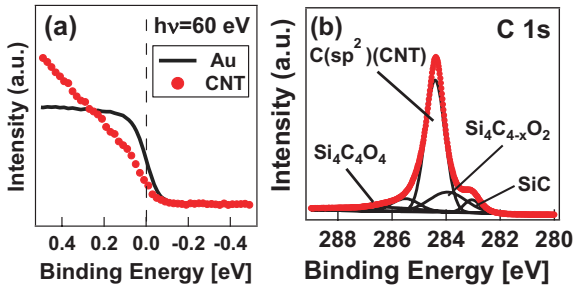

Fig. 1. PES spectra of (a) VBM of CNTs with the Fermi edge of Au (hν = 60 eV), and (b) C 1s core spectrum of CNT(several nm)/4H-SiC (hν = 350 eV).

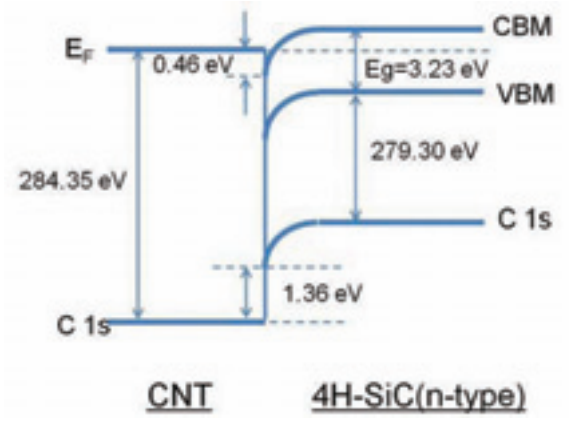

Fig. 2. Band alignment of CNT/n-type 4H-SiC heterojunction.

[1] M. Kusunoki *et al.*, Appl. Phys. Lett. **77** (2000) 531.
[2] M. Kusunoki *et al.*, Chem. Phys. Lett. **366** (2002) 458.
[3] T. Maruyama, S. Sakakibara, H. Ito, H. Yamane, E. Shigemasa and N. Kosugi, UVSOR Activity Report **38** (2011) 127.
[4] S. Sakakibara, Unpublished master's thesis. Meijo University (2012).

BL6U

Valence-Band Dispersion of Metal Phthalocyanines (I): *Intra*molecular and *Inter*molecular Electron-Phonon Coupling in Crystalline Films of Zinc Phthalocyanine (ZnPc)

H. Yamane and N. Kosugi

Department of Photo-Molecular Science, Institute for Molecular Science, Okazaki 444-8585, Japan
School of Physical Sciences, The Graduate University for Advanced Studies, Okazaki 444-8585, Japan

It has been predicted by theoretical studies that local/nonlocal electron-phonon (e-ph) couplings play a crucial role in the charge transport mechanism in organic molecular solids [1]. In order to examine the evidence for the e-ph coupling in organic molecular solids experimentally, the temperature dependence of the electronic structure of well-crystallized samples should be taken into account.

In this work at BL6U, we prepared a crystalline film of zinc phthalocyanine (ZnPc), a promising material for organic electronics, with a flat-lie orientation on the Au(111) surface, wherein the intermolecular π-π interaction exists along the surface normal direction. The crystallinity of the ZnPc film was confirmed by the incident-angle dependence of X-ray absorption spectroscopy, the low-energy electron diffraction, and the CuKα X-ray diffraction. From the angle-resolved photoemission spectroscopy (ARPES) experiments on the crystalline ZnPc film on Au(111), we observed an intermolecular valence-band dispersion [$E(\boldsymbol{k})$] and the clear evidence for the e-ph coupling as a function of the temperature.

Figure 1 (a) shows the $E(\boldsymbol{k})$ relation of the ZnPc crystalline film prepared on Au(111), which is obtained from the incident photon energy dependence of normal emission ARPES spectra at 15 K. The highest occupied molecular orbital [HOMO (π, a_{1u})], Zn3d (b_{1g}), and π's derived peaks show a dispersive shift with the same periodicity. This periodicity corresponds well with the Γ and Y points, estimated from the lattice constant of 3.32 Å determined by the X-ray diffraction [Fig. 1 (b)]. This correspondence indicates that the observed $E(\boldsymbol{k})$ is ascribed to the intermolecular interaction. The tight-binding fitting to the $E(\boldsymbol{k})$ relation gives a HOMO transfer integral (t) of 25 meV and hence a HOMO bandwidth (= 4t) of 100 meV, which is the same order as a reorganization energy for local phonons of CuPc [2].

In order to examine the e-ph coupling in crystalline ZnPc film, we measured the temperature dependence of ARPES at the Γ and Y points with the 60 and 90 eV incident photons, respectively. As seen in Fig. 1 (c), the Γ-point HOMO energy shifts depending on the temperature, while the Y-point HOMO energy seems independent on the temperature. From the lineshape analysis, we found that both the HOMO bandwidth (i.e., energy difference between the Γ- and Y-HOMO) and the Γ-HOMO peakwidth are narrowed with increasing the temperature, which is an opposite trend in a remanent Au(111) Fermi edge. This is the distinct indication of the local/nonlocal e-ph interaction; that is, band narrowing due to the interaction with local phonons (intramolecular vibrations) and band widening due to interaction with nonlocal phonons (intermolecular lattice vibrations) [1]. Thus, it is considered that a transition between incoherent hopping transport associated with the local e-ph coupling and coherent band transport associated with the nonlocal e-ph coupling occurs within the energy scale of 100 meV in the crystalline ZnPc. From the $E(\boldsymbol{k})$ relation, in the coherent band transport at the low temperature, the effective mass and the mobility of the HOMO hole are 13.8m_0 and 28.9 cm^2/Vs at 15 K, respectively.

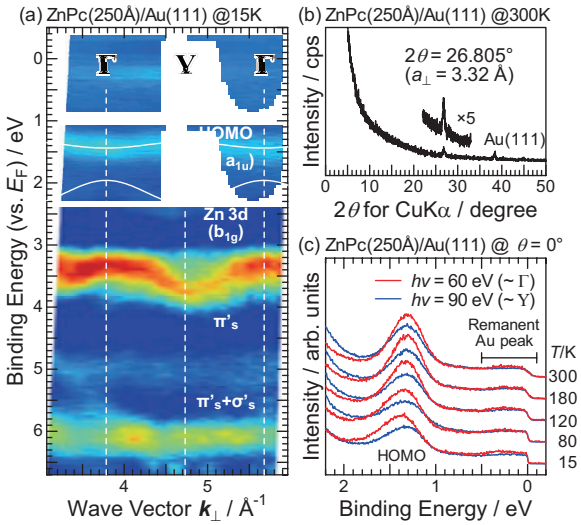

Fig. 1. (a) Intermolecular $E(\boldsymbol{k})$ relation of the crystalline ZnPc film on Au(111) at 15 K, wherein the second derivative of the ARPES spectra were used for mapping out. White curves for the HOMO and Zn 3d derived bands are the best-fit results in the tight-binding model. (b) CuKα X-ray diffraction of the crystalline ZnPc film on Au(111) at 300 K. (c) Temperature dependence of ARPES in the HOMO-band region at the Γ and Y points, measured with 60 and 90 eV incident photons, respectively.

[1] C. A. Perroni, V. M. Ramaglia, and V. Cataudella, Phys. Rev. B **84** (2011) 014303, and refs therein.
[2] S. Kera, H. Yamane, and N. Ueno, Prog. Surf. Sci. **84** (2009) 135.

Valence-Band Dispersion of Metal Phthalocyanines (II): Phase Reversal of the Intermolecular HOMO-Band Dispersion between Crystalline Films of Non- and Per-Fluorinated Zinc Phthalocyanines

H. Yamane and N. Kosugi

Department of Photo-Molecular Science, Institute for Molecular Science, Okazaki 444-8585, Japan
School of Physical Sciences, The Graduate University for Advanced Studies, Okazaki 444-8585, Japan

The energy band dispersion [$E(\boldsymbol{k})$] is a fundamental basis to understand electric properties of solids such as hole mobility (μ_h). In the field of organic solids, the study of the intermolecular $E(\boldsymbol{k})$ shows a rapid progress due to the needs of the interpretation of the charge transport mechanism in organic electronic devices. However, due to the weak intermolecular interaction and the difficulty in preparing crystallized films for the $E(\boldsymbol{k})$ measurement, the intermolecular $E(\boldsymbol{k})$ has been observed for high-μ_h materials. In order to elucidate and control the functionality of organic semiconductors, a systematic experiment on the intermolecular $E(\boldsymbol{k})$ can play a crucial role.

Recently, we have observed the intermolecular $E(\boldsymbol{k})$ in a crystalline zinc phthalocyanine (ZnPc) film on Au(111) using the angle-resolved photoemission spectroscopy (ARPES) at BL6U [1]. One of the key points of this observation is that the $E(\boldsymbol{k})$ relation of ZnPc can be a benchmark for the systematic study on the intermolecular interaction in terms of the intermolecular distance and/or the orbital symmetry by changing terminal groups or central metals in the molecule. In this work, we have studied the effect of the fluorination of ZnPc (*i.e.*, F_{16}ZnPc) on the $E(\boldsymbol{k})$.

Figure 1 (a) and (b) show the *ex situ* CuKα X-ray diffraction (XRD) and the *in situ* incident-angle (α) dependence of N-K X-ray absorption spectra (XAS), taken by the sample-current mode, measured for a 150-Å-thick F_{16}ZnPc film on Au(111), respectively. A F_{16}ZnPc-derived XRD peak appears at 2θ = 27.565°, which gives a lattice constant of 3.23 Å. This value is in good agreement with the molecular orientation estimated from XAS, wherein the sharp π^* peaks at 397–400 eV are strongest at α = 60°. From these results, we found that the molecules form a well-known β-bilayer (β_{BL})-crystalline structure, which is similar to α-crystalline ZnPc, with their molecular plane parallel to the Au(111) surface.

Figure 1 (c) shows the incident photon energy ($h\nu$) dependence of ARPES at the normal emission for the β_{BL}-crystalline F_{16}ZnPc film on Au(111). A highest occupied molecular orbital (HOMO)-derived peak shows a clear periodic shift with $h\nu$. From the $E(\boldsymbol{k})$ relation for the HOMO band of F_{16}ZnPc and ZnPc in Fig 1 (d), we found that the bandwidth of F_{16}ZnPc (120 meV) is larger than that of ZnPc (100 meV), which is consistent with their intermolecular distance. Moreover, the dispersion phase for the HOMO band of F_{16}ZnPc is flipped from that of ZnPc. This reversal may originate from the π···F 2p interaction, which is under theoretical consideration.

[1] H. Yamane and N. Kosugi, a separate page in this volume.

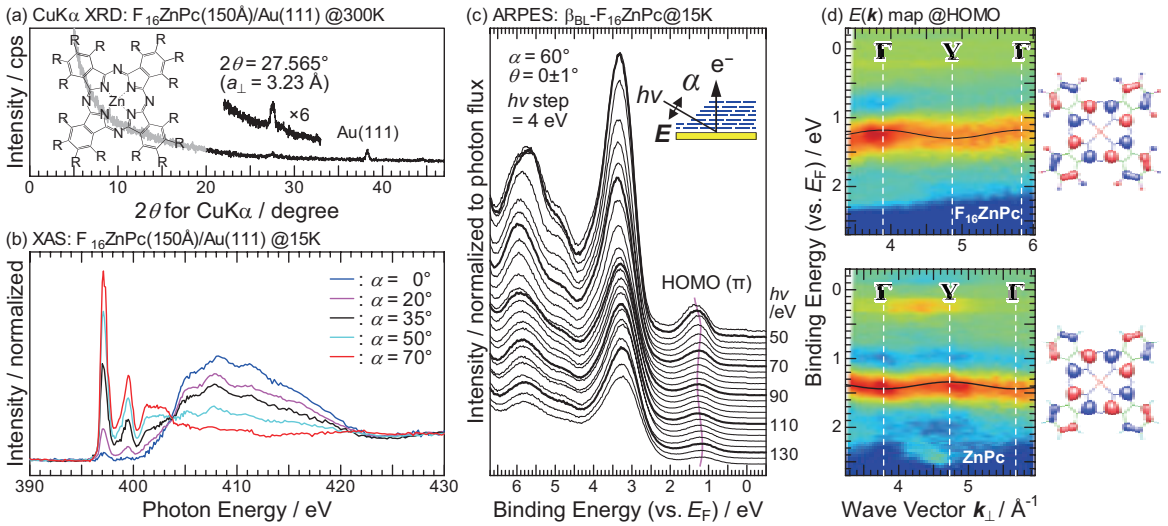

Fig. 1. (a) CuKα XRD of F_{16}ZnPc films (150 Å) on Au(111). Inset is a molecular structure of ZnPc (R = H) and F_{16}ZnPc (R = F). (b) Incident-angle (α) dependence of N-K X-ray absorption spectra for the crystalline film of F_{16}ZnPc on Au(111) at 15 K. (c) Photon energy ($h\nu$) dependence of ARPES for the crystalline film of F_{16}ZnPc on Au(111) at 15 K. (d) Comparison of the HOMO-band dispersion of β_{BL}-F_{16}ZnPc (top) and α-ZnPc (bottom).

Valence-Band Dispersion of Metal Phthalocyanines (III): Dimerization of Mn-3d-Derived Band in Crystalline Films of Manganese Phthalocyanine (MnPc)

H. Yamane and N. Kosugi

Department of Photo-Molecular Science, Institute for Molecular Science, Okazaki 444-8585, Japan
School of Physical Sciences, The Graduate University for Advanced Studies, Okazaki 444-8585, Japan

Metal phthalocyanines (MPc) have attracted much attention due to their unique electronic and magnetic properties in terms of organic electronics/spintronics. In this work, we have examined the intermolecular interaction in a crystalline film of MnPc, a promising organic spintronic material, by using angle-resolved photoemission spectroscopy (ARPES) at BL6U.

Figure 1 (a) shows the CuKα X-ray diffraction (XRD) for a 200-Å-thick MnPc film on Au(111). A MnPc-derived XRD peak appears at 2θ = 27.250°, which gives a lattice constant of 3.27 Å. In the N-K X-ray absorption spectra (XAS) for the crystalline MnPc film on Au(111) [Fig. 1 (b)], sharp transition peaks appear at 397–403 eV. Among these, peak X at 398 eV shows a broad incident angle (α) dependence, which may originate from the hybridization between the N p and Mn d states. Other peaks are ascribed to the N 1s → π* transitions. A sharp α dependence of these π* peaks indicates the flat-lie orientation, which is consistent with XRD.

Figure 1 (c) shows the incident photon energy ($h\nu$) dependence of ARPES at the normal emission for the crystalline MnPc film prepared on Au(111) at 15 K. The highest occupied molecular orbital (HOMO) of ZnPc is derived from the C 2p orbital; on the other hand, the HOMO of MnPc is derived from the Mn 3d orbital [1]. The HOMO (Mn 3d) and HOMO-1 (C 2p) derived peaks of MnPc show a clear periodic shift with $h\nu$. Moreover, we have found that the Mn 3d derived peak consists of two components with the different dispersion, indicating the relatively strong interaction at the Mn site.

Figure 1 (d) shows the valence band dispersion $E(\boldsymbol{k})$ map for the crystalline MnPc film on Au(111), wherein the symmetric Γ and Y points are estimated from the lattice constant of 3.27 Å from the XRD data. The agreement between the periodicity of C 2p peak and the symmetric points indicates that the observed $E(\boldsymbol{k})$ is ascribed to the intermolecular interaction. For the Mn 3d peak, the peak split and its dispersion are clearly seen in the $E(\boldsymbol{k})$ map. Furthermore, the periodicity of the Mn 3d dispersion is 1/2 times of that of the C 2p dispersion as labeled Y_{2a}. A possible origin of the Mn 3d dispersion is dimerization of the Mn d_π state.

Moreover, various band dispersions are observed in the energy region of 3–4 eV. There is a possibility of the deconvolution of the broad photoemission peak into individual molecular orbitals by the combination with theoretical calculations.

[1] *e.g.*, M.-S. Liao and S. Scheiner, J. Chem. Phys. **114** (2001) 9780; M.-S. Liao, J.D. Watts and M.-J. Huang, Inorg. Chem. **44** (2005) 1941.

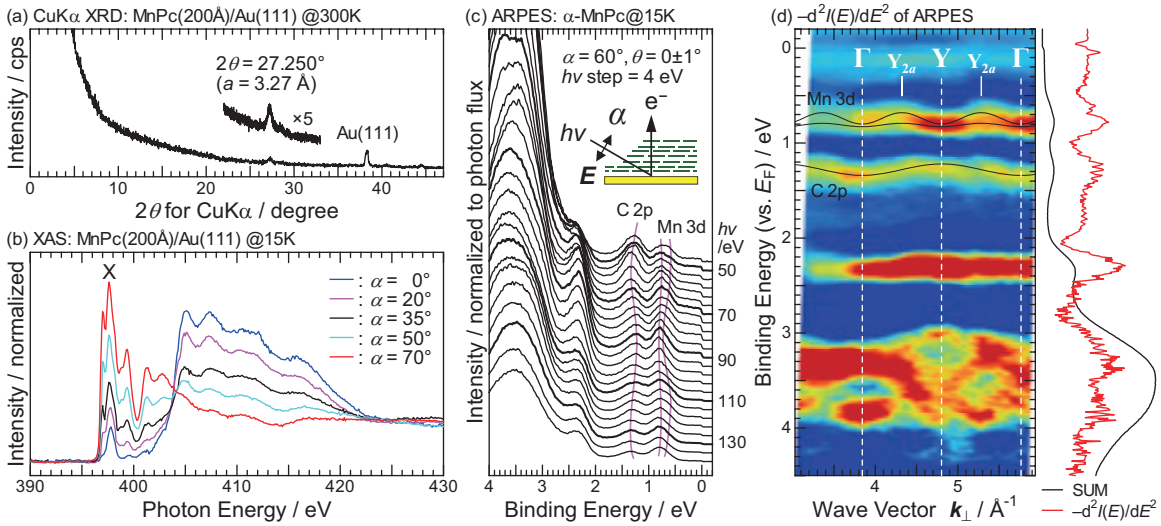

Fig. 1. (a) CuKα XRD of MnPc films (200 Å) prepared on Au(111). (b) The incident angle (α) dependence of N K-edge XAS of crystalline films of MnPc on Au(111) at 15 K. (c) The photon energy ($h\nu$) dependence of ARPES and (d) the intermolecular $E(\boldsymbol{k})$ relation, which is obtained from the second derivative of the raw ARPES data, of the crystalline film of MnPc prepared on Au(111) at 15 K.

BL6B

Far-Infrared Reflective Study of Alkali Niobate Ceramics

T. Nishi, T. Hayakawa, H. Yamada and K. Kakimoto
Graduate School of Engineering, Nagoya Institute of Technology Nagoya 466-8555, Japan

Alkali niobate is one of the promising candidates of lead-free piezoelectric materials. Especially, Li-doped (Na,K)NbO_3 (LNKN) solid solution shows excellent piezoelectric properties. Although it was expected that the distortion of NbO_6 unit would contribute to the good ferroelectric properties, the details are still unclear. Thus, the knowledge of the relation between the vibration of NbO_6 unit and ferroelectric properties is strongly needed. The vibration of the NbO_6 is observed as a ferroelectric soft mode in the infrared (IR) spectrum. So, this study was aimed to the analysis of the ferroelectric soft mode of $Na_{0.5}K_{0.5}NbO_3$ which is a base material of the LNKN.

The $Na_{0.5}K_{0.5}NbO_3$ ceramic sample was synthesized by a solid-state reaction method. The surface of $Na_{0.5}K_{0.5}NbO_3$ ceramic was polished and used for IR reflectivity study. The reflectivity far-infared spectram was obtained in the range of 20 – 8000 cm^{-1} at room temperature using a synchrotron radiation source, then the spectra were corrected by using a Michelson interferometer (Bruker, IFS66v).

Figure 1 shows the reflectance spectram of $Na_{0.5}K_{0.5}NbO_3$ ceramics at room temperature. The spectrum was analyzed using the following formula,

$$\varepsilon(\omega) = \varepsilon_\infty \prod_{j=1}^{n} \frac{\omega_{jLO}^2 - \omega^2 + i\omega\gamma_{jLO}}{\omega_{jTO}^2 - \omega^2 + i\omega\gamma_{jTO}} \qquad (1).$$

Figure 2 shows the infrared reflectance spectram around the wavenumber of the soft mode and the fitting curve. Table 1 shows the fitting parameters of the soft mode. The soft mode frequency obtained from the IR spectroscopic analysis was 255 cm^{-1}. Relative permittivity ε_r calculated from the soft mode wavenumber was ε_r of 520. This result was different from the measured value (capacitance method, ε_r of 555 at 1kHz). The permittivity in the range of THz, which was the observed soft mode, is contributed a ionic polarization. On the other hand, the permittivity in the range of kHz was due to ionic and orientation polarizations. This suggested that the ionic polarization contributed the NbO_6 unit accounted for 94 % of the total permittivity of $(Na_{0.5}K_{0.5})NbO_3$. Thus, the relation between the distortion of the NbO_6 units and a ferroelectric property can be evaluated by using the IR spectroscopy analysis. We will investigate the relation between a ferroelectric property and the amount of a distortion of the NbO_6 by analyzing the IR spectra of Li-doped (Na,K)NbO_3 solid solution.

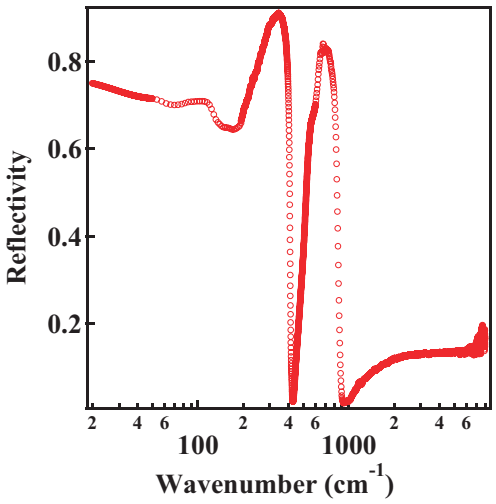

Fig. 1. Infrared reflectance spectra of $Na_{0.5}K_{0.5}NbO_3$ ceramics at R.T..

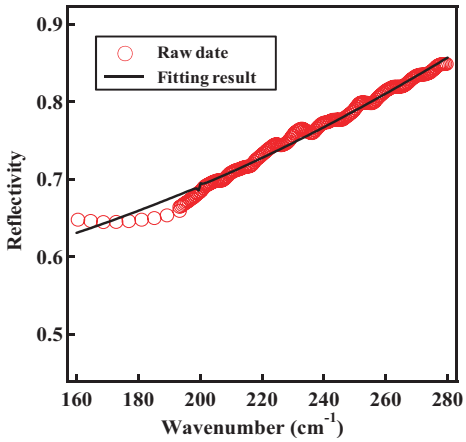

Fig. 2. Infrared reflectance spectra around the soft mode.

Table 1. Fitting parameters of the soft mode.

Fitting parameter	IR
ω_{TO}	254.51
ω_{LO}	434.34
γ_{TO}	163.80
γ_{TO}	568.14

This research was supported by the Industrial Technology Research Grant Program in 2007 from the New Energy and Industrial Technology Development Organization (NEDO) of Japan.

BL7B

Luminescence Decay of Organic-Inorganic Perovskite Compounds

M. Koshimizu, N. Kawano and K. Asai

Department of Applied Chemistry, Graduate School of Engineering, Tohoku University, Sendai 980-8579, Japan

Quantum confinement in semiconductors has been a subject of great interest from the viewpoint of the applications for optical devices, as well as the basic science. Among various materials having low-dimensional quantum confinement structure, Pb-based organic-inorganic perovskite-type compounds have attracted much attention due to their unique optical properties. The crystal of these compounds composed of alternating inorganic and organic layers. The inorganic and organic layers are composed of PbX_6^{2-} octahedra and organic amine, respectively. Due to the large difference in band-gap energy and dielectric constant in the organic and inorganic layers, an exciton in the inorganic layer is tightly confined, resulting in huge binding energy (several hundreds of meV) and large oscillator strength.

We have been developing scintillation materials using these compounds. In recent years, the demand for fast scintillation materials has increased for applying in radiation detectors with an excellent timing property and the ability to operate at a high counting rate. The large binding energy and oscillator strength of the exciton enables us to fabricate scintillation materials with excellent timing response [1]. During the course of the development, we found that the scintillation properties largely depend on the amine molecules used in the organic layer, in which no luminescence or scintillation occurs. In order to reveal the origin of this dependence, the luminescence decay characteristics should be obtained under excitation (1) only in the inorganic layers and (2) both in the inorganic and the organic layers. In this report, we show that the excitation in the organic layers has little influence on the luminescence behavior.

The chemical formula of the sample compound is $(C_6H_5C_2H_4NH_3)_2PbBr_4$. The single crystals of the compound were grown by solvent diffusion technique. The photoluminescence spectra and time profiles were measured using vacuum ultraviolet (VUV) light as an excitation source at UVSOR BL7B operated in single bunch mode.

Figure 1 shows the photoluminescence spectrum. The prominent peak at 410 nm is ascribed to free excitons. A small shoulder at 440 nm may be ascribed to excitons trapped at some defects or impurities, because the intensity of this shoulder has been different in different crystals. The shape of the spectra was quite similar for the excitation wavelength range of 50 – 300 nm.

Figure 2 shows the photoluminescence time profiles at 410 nm under excitation at 300 nm and 180 nm. In the case of the excitation at 180 nm, both the inorganic layer and the organic layer were excited. The decay characteristics were also quite similar. Hence, these results indicate that the excitation in the organic layer has little influence on the luminescence and scintillation behavior.

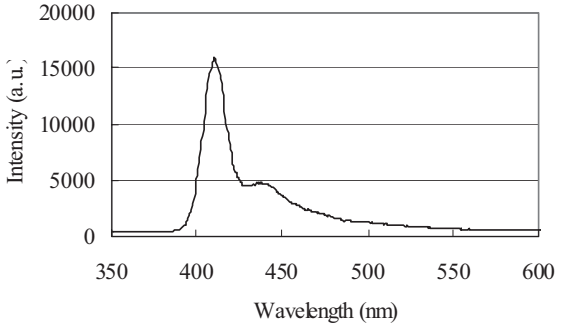

Fig. 1. Luminescence spectrum of the sample excited at 300 nm.

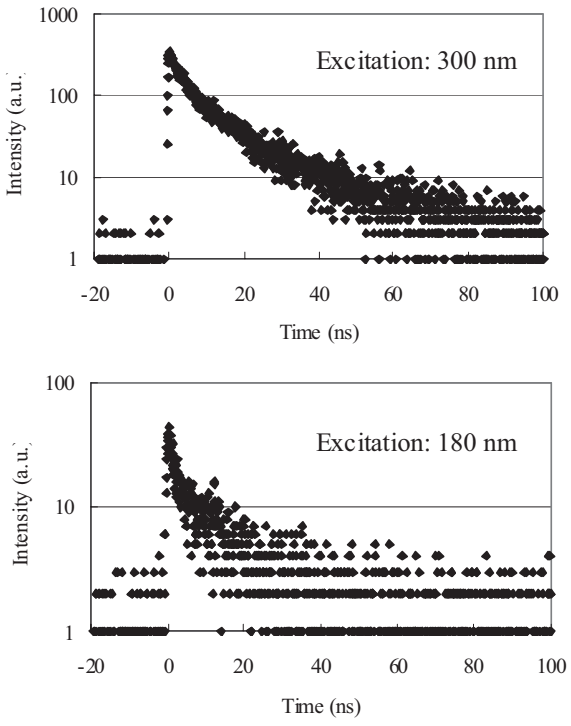

Fig. 2. Luminescence time profiles at 410 nm.

[1] K. Shibuya *et al.,* Appl. Phys. Lett. **84** (2004) 4370.
[2] K. Shibuya *et al.,* Jpn. J. Appl. Phys. Part2 (Express Letter) **43** (2004) L1333.
[3] S. Kishimoto *et al.,* Appl. Phys. Lett. **93** (2008) 261901.

BL7B

Photoluminescence upon Vacuum Ultraviolet Excitation in Pr^{3+} ion doped Inorganic Materials

Y. Inaguma, H. Horiguchi, S. Sasaki and D. Mori
Department of Chemistry, Faculty of Science, Gakushuin University, Tokyo 171-8588, Japan

Pr^{3+} ion doped inorganic materials has been extensively investigated in relation with various applications [1]: laser materials utilizing visible emission from the $^3P_0$ and $^1D_2$ states (blue-green and red emission, respectively), or infrared emission from the $^1G_4$ state of Pr^{3+}, field emission display (FED) devices utilizing red $^1D_2$ emission, scintillators or tunable ultraviolet (UV) lasers utilizing UV emission from the 4f5d state. The emission color or energy in Pr^{3+} ion doped inorganic materials is strongly related to the electronic structure, especially, the band gap energy of host materials. Therefore the emission color can be controlled by the choice of host materials [2].

Recently phosphor materials emitting UV light upon vacuum ultra violet (VUV) excitation are desired as the substitutes of mercury lamp due to the toxicity of mercury. As mentioned above, since the UV emission from the 4f5d state in Pr^{3+} can be observed, Pr^{3+} ion doped compounds are expected to be candidates of the UV phosphors. The UV emission from the 4f5d state would be observed when the band gap energy of the host material is in the VUV region. In this study we then chose Pr^{3+} ion doped alkaline-earth phosphates with the band gap energy in the VUV region and investigated their luminescence properties. Herein, we report on the photoluminescence upon VUV excitation of $Ca_3(PO_4)_2$:Pr among them.

The polycrystalline samples were synthesized by a conventional solid state reaction at elevated temperature. The mixture of starting materials: alkaline-earth carbonate such as $CaCO_3$, $(NH_4)H_2PO_4$ and Pr nitrate solution were calcined at 1000°C in air. The calcined powder was pressed into pellets and sintered at 1000-1200°C in air. The phase identification for the samples was carried out by the laboratory powder X-ray diffraction (XRD) using a Rigaku RINT 2100 diffractometer with a Bragg Brentano geometry (graphite-monochromatized CuKα radiation). The emission and excitation spectra were recorded in the beamline BL7B at the UVSOR facility.

The obtained sample was crystallized to be the hexagonal β-type form of tricalcium phosphates composed of isolated PO_4 tetrahedra and Ca^{2+} ions, which was confirmed by a powder XRD experiment. Figure 1 shows the emission spectrum upon excitation of 173 nm (right side) and excitation spectrum emission monitored at 280 nm (left side) for $Ca_3(PO_4)_2$:Pr 2% at room temperature. Here, the emission spectrum was not corrected, while the excitation spectrum was corrected for the spectral distribution of excitation light source. As seen in Fig. 1, the UV emission peaks at 240 and 280 nm were observed, which correspond to the transitions from the 4f5d state to the $4f^2$ (^3H_J) state of Pr^{3+}. In the excitation spectrum, the peaks around 175 nm and 200-220 nm were observed, which correspond to the host absorption band, i.e. the intra charge transfer of PO_4^{3-}[3] and the transition from the ground state of $4f^2$($^3H_4$) to the 4f5d state of Pr^{3+}, respectively.

It was found that $Ca_3(PO_4)_2$:Pr exhibits the UV emission corresponding to the transition from the 4f5d state of Pr^{3+} and the Pr^{3+} ion doped alkaline–earth phosphates are candidates of UV phosphors.

The luminescence properties upon VUV excitation in other Pr^{3+} ion doped alkaline phosphate will be reported in the near future.

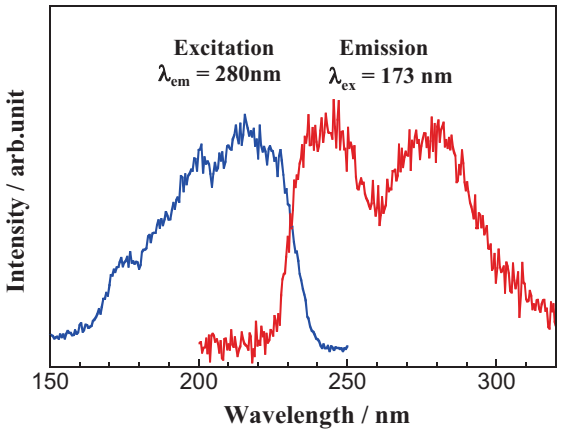

Fig. 1. Emission spectrum upon excitation of 173 nm (right side) and excitation spectrum emission monitored at 280 nm (left side) for $Ca_3(PO_4)_2$:Pr 2% at room temperature.

The authors thank Mr. M. Hasumoto and Prof. S. Kimura for their experimental supports and helpful advices.

[1] E. Van der Kolk *et al.*, Phys. Rev. B **64** (2001) 195129.
[2] Y. Inaguma *et al.*, Inorg. Chem. **50** (2011) 5389.
[3] H. Ling *et al.*, J. Solid State Chem. **177** (2004) 901.

BL8B

Photoelectron Spectrum of Zn-Phthalocyanine/C_{60} Interface under the Light Irradiation

S. Tanaka, K. Fukuzawa and I. Hiromitsu

Interdisciplinary Faculty of Science and Engineering, Shimane University, Matsue 690-8504 Japan

The electronic structure at the organic/organic and organic/metal interfaces plays an important role for the photovoltaic properties of the organic solar cell (OSC). The photoelectron spectroscopy is the one of the powerful methods to investigate the electronic structure of the organic/organic and organic/metal interfaces [1]. We have recently reported the electronic structures of the organic thin films under the light irradiation which were investigated by using the photoelectron spectroscopy with an external light source. In the previous report, we reported the photoinduced shift in the photoelectron spectra of the Zinc-phthalocyanine (ZnPc)/C_{60} interface [2]. The shift direction of the photoelectron spectrum was corresponded to the polarity of the photovoltaic effect at the ZnPc/C_{60} interface. In this report, the progress of the experimental results of the photoelectron shift under the light irradiation is reported.

The organic films were fabricated by the vacuum deposition technique. Two kinds of sample were fabricated: the planer hetero-junction (PHJ) sample and the bulk hetero-junction (BHJ) sample. The PHJ sample had a planer interface of ZnPc and C_{60} on the indium-tin oxide substrate. The BHJ sample was fabricated by the co-deposition of ZnPc and C_{60}. For the observation of the photoinduced effect on the electronic structure, the photoelectron spectra under the light irradiation were compared with that under dark. A solar simulator was used as the light source for the irradiation. The simulated airmass 1.5 solar illumination was exposed to the sample in a vacuum chamber through a viewport. All the photoelectron measurements were carried out with a photon energy of 40 eV at room temperature.

The photoelectron spectrum of the ZnPc/C_{60} interface was shifted toward higher kinetic energies by the light irradiation (Fig.1 (a)). The C_{60} thickness dependence of the photoinduced shift on the photoelectron spectrum is shown in Fig. 1 (b). The shift value was saturated at around 10nm of the C_{60} layer thickness and was approximately 60 meV. The photoinduced shift was caused by the photovoltaic effect at the ZnPc/C_{60} interface. The photogenerated electrons were accumulated in the C_{60} layer, causing the acceleration of the photoelectrons (Fig. 1(b) inset). The increase of the shift value in the initial stage of the C_{60} deposition was probably related to the increase of the interfacial area of the ZnPc/C_{60}. However, the saturated shift value of 60 meV was approximately one order smaller than the open circuit voltage of the ZnPc/C_{60} PHJ OSC. The reason of this discrepancy is still an open question.

It is known that the OSC with a BHJ layer shows higher energy conversion efficiency than that with a PHJ OSC [3]. However, the photoelectron spectrum of ZnPc:C_{60} (volume ration = 1:1) BHJ sample showed no significant photoinduced shift under the light irradiation. The present results indicate that semipermeable membranes for the electric charges are required on both sides of the BHJ layer to generate a charge current flowing in the OSC.

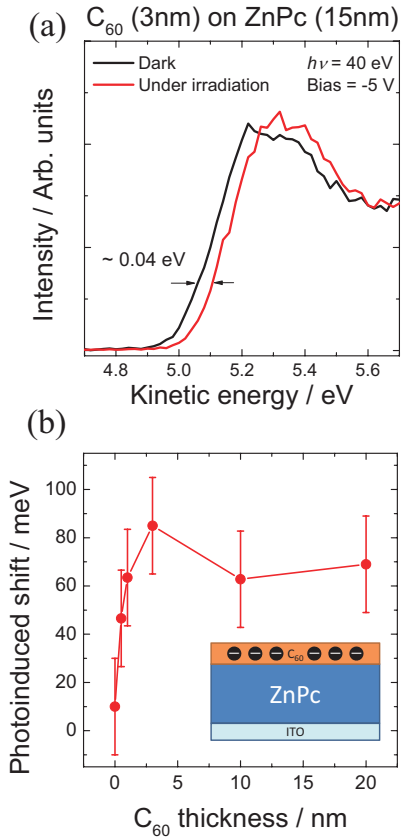

Fig. 1. (a) Photoelectron spectra of the C_{60} (3 nm) on the ZnPc layer at the secondary electron cutoff region. The red (black) curve indicates the photoelectron spectrum under the light irradiation (dark). (b) C_{60} thickness dependence of the photoinduced shift of the photoelectron spectrum. Inset shows the schematic image of the charge distribution at the sample surface under the light irradiation.

[1] H. Ishii *et al.*, Adv. Mater. **11**(1999) 605.
[2] S. Tanaka *et al.*, UVSOR Activity Report **38** (2010) 136.
[3] T. Taima *et al.*, Appl. Phys. Lett. **85** (2004) 6412.

BL8B

Influence of Growth Conditions on the Interface Electronic Structure at Planar Organic Donor/Acceptor Heterojunctions of Sexithiopheneand C_{60}

U. Hörmann[1], Y. Nakayama[2], Y. Ozawa[3], W. Brütting[1] and H. Ishii[2, 3]
[1]*Institute of Physics, University of Augsburg, Augsburg 86135, Germany*
[2]*Center for Frontier Science, Chiba University, Chiba 263-8522, Japan*
[3]*Faculty of Engineering, Chiba University, Chiba 263-8522, Japan*

On the way to high performance organic solar cells tremendous effort has been put into increasing the short circuit current by structural device optimization. Little attention has, however, been paid to the influence of morphology on the open circuit voltage (V_{oc}).

Here we investigate the electronic structure at sexithiophene (6T)/C_{60} hetero interfaces under different preparation conditions. In solar cells this system yields a V_{oc} of 0.5 V for room temperature grown films. Accompanied by morphological changes, this voltage is reduced to 0.37 V if C_{60} is deposited onto a high temperature grown 6T film.

In high vacuum 6T layers of 10 nm and 5 nm thickness have been deposited onto PEDOT:PSS (Clevios AI4083) covered indium tin oxide substrates at substrate temperatures of 100 °C (HT) and 30 °C (RT), respectively. In both cases, the deposition rate was set to 0.3 – 0.8 Å/s. C_{60} was deposited stepwise onto the 6T films at a rate of 0.3 Å/s at room temperature. Ultraviolet photoelectron spectroscopy (UPS) was performed at BL8B at UVSOR. The photon energy, incident angle and photoelectron emission angle were set to 30 eV, 45° and 0°, respectively throughout this study. For valence-band region (VB) spectra a bias of +5 V was applied to the sample in order to avoid charging, whereas -13 V wasapplied for secondary electron cutoff (SECO) measurements.

As expected from previous studies, heating in vacuum increases the work function of PEDOT:PSS, from 5.0 eV to 5.3 eV. Figure 1 shows the recorded UPS spectra of the 6T films and C_{60} overlayers on them. For direct comparison RT (black) and HT (red) data are shown in one plot. Both the SECO and VB spectra of the neat 6T film remain energetically unchanged by substrate heating. However, the features become sharper for the HT grown film. This can probably be attributed to the presence of two different crystalline 6T phases in the RT film as indicated by x-ray diffraction (XRD) measurements [1].

Interestingly the whole spectrum (VB and SECO) is shifted by $\Delta = 0.12$ eV towards higher binding energies, when 0.3 nm of C_{60} are deposited onto the HT 6T film. This indicates the occurrence of band bending at the C_{60}/6T(HT) interface as illustrated in Figure 2. By contrast, no band bending is observed in the RT case, where the energetic position of the overall spectrum remains unchanged by 0.3 nm of C_{60} (even though the HOMO onset shows a slight downshift due to spectral broadening).

In both cases the SECOs shift towards higher vacuum level energies with increasing C_{60} coverage. This can possibly be ascribed to mutual polarization of the molecules.The RT shift of +0.15 eV is in accordance with Ref. [2]. In the HT case the vacuum level recovers to the neat 6T value of 4.6 eV. Note, however, that 6T features are still present in the VB spectrum in this case. This suggests that the SECO shift probably has not reached its maximum and might stem from an incomplete C_{60} coverage on the extremely rough 6T(HT) surface observed by AFM.

Comparison of the 5 nm VB spectra reveals that growing C_{60} on HT 6T shifts the C_{60} HOMO to larger binding energies from 1.9 eV to 2.0 eV. This shift results in a reduction of the 6T/C_{60} charge transfer gap for the HT sample (indicated in Fig.2), which is in accordance with the reduced V_{oc} observed for 6T(HT)/C_{60} solar cell devices.

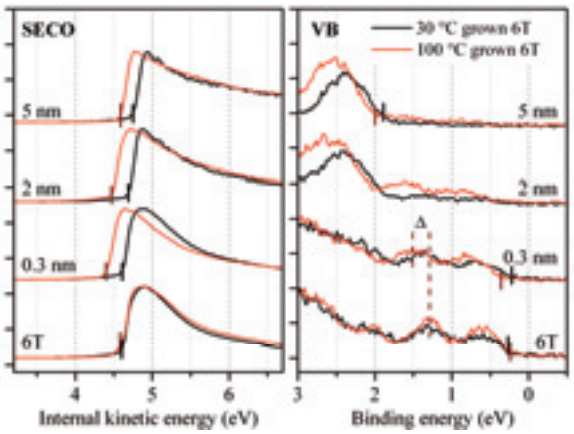

Fig.1. SECO (left) and VB (red) spectra of C_{60} grown on the RT (black) and HT (red) grown 6T.

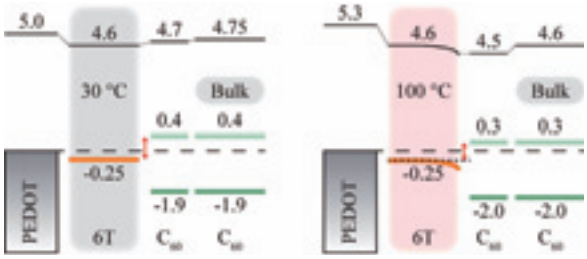

Fig.2. Schematic energy diagram of C_{60} grown on RT (left) and HT (right) grown 6T. Values are energy relative to the PEDOT:PSS Fermi level (units: eV).

[1] A. Hinderhofer and F. Schreiber (UniTübingen), unpublished.
[2] A. Wilke and N. Koch (HU Berlin), *in prep*.